

# p14<sup>ARF</sup> forms meso-scale assemblies upon phase separation with NPM1

Received: 26 November 2023

Accepted: 25 October 2024

Published online: 11 November 2024

 Check for updates

Eric Gibbs<sup>1</sup>, Qi Miao<sup>1</sup>, Mylene Ferrolino <sup>1</sup>, Richa Bajpai<sup>2</sup>, Aila Hassan<sup>3</sup>, Aaron H. Phillips<sup>1</sup>, Aaron Pitre <sup>4</sup>, Rainer Kümmerle<sup>3</sup>, Shondra Miller <sup>2</sup>, Gergely Nagy <sup>5</sup>, Wellington Leite<sup>5</sup>, William Heller <sup>5</sup>, Chris Stanley <sup>6</sup>, Barbara Perrone<sup>3</sup> & Richard Kriwacki <sup>1,7</sup> 

NPM1 is an abundant nucleolar chaperone that, in addition to facilitating ribosome biogenesis, contributes to nucleolar stress responses and tumor suppression through its regulation of the p14 Alternative Reading Frame tumor suppressor protein (p14<sup>ARF</sup>). Oncogenic stress induces p14<sup>ARF</sup> to inhibit MDM2, stabilize p53 and arrest the cell cycle. Under non-stress conditions, NPM1 stabilizes p14<sup>ARF</sup> in nucleoli, preventing its degradation and blocking p53 activation. However, the mechanisms underlying the regulation of p14<sup>ARF</sup> by NPM1 are unclear because the structural features of the p14<sup>ARF</sup>-NPM1 complex were elusive. Here we show that p14<sup>ARF</sup> assembles into a gel-like meso-scale network upon phase separation with NPM1. This assembly is mediated by intermolecular contacts formed by hydrophobic residues in an  $\alpha$ -helix and  $\beta$ -strands within a partially folded N-terminal portion of p14<sup>ARF</sup>. These hydrophobic interactions promote phase separation with NPM1, enhance p14<sup>ARF</sup> nucleolar partitioning, restrict NPM1 diffusion within condensates and nucleoli, and reduce cellular proliferation. Our structural analysis provides insights into the multifaceted chaperone function of NPM1 in nucleoli by mechanistically linking the nucleolar localization of p14<sup>ARF</sup> to its partial folding and meso-scale assembly upon phase separation with NPM1.

Arf (Alternative Reading Frame; p14<sup>ARF</sup> in human, p19<sup>Arf</sup> in mouse) is an intrinsically disordered protein and key tumor suppressor that is lost or silenced in most human cancers. Arf is induced in response to oncogene activation, *e.g.*, Myc and Ras signaling, and binds MDM2, an E3 ubiquitin ligase for p53, leading to MDM2 inhibition, p53 stabilization and cell cycle arrest<sup>1</sup>. In proliferating cells, Arf is maintained at low levels and localizes to the granular component (GC) of the nucleolus through its interaction with Nucleophosmin (NPM1)<sup>2,3</sup>. Interactions with NPM1 in the nucleolus are critical for regulating Arf stability and function. By binding Arf in the nucleolus, NPM1 protects

Arf from proteasomal degradation in the nucleus<sup>4–8</sup>. Release from NPM1 facilitates Arf targeting of MDM2 in the nucleus<sup>9</sup> and occurs in response to various stressors, including DNA damage<sup>7,10</sup> and nucleolar disruption<sup>11,12</sup>. Furthermore, induced p19<sup>Arf</sup> expression induces NPM1 degradation<sup>13</sup> and redistribution of HDM2 into nucleoli<sup>14</sup>.

Nucleoli are liquid-like membrane-less organelles (MLOs) assembled in part through liquid-liquid phase separation (LLPS)<sup>15,16</sup>. NPM1 forms pentamers and mediates the assembly of the GC in part through multivalent interactions of acidic tracts (A-tracts) within its central intrinsically disordered region (IDR) with multivalent arginine-rich

<sup>1</sup>Department of Structural Biology, St. Jude Children's Research Hospital, Memphis, Tennessee, USA. <sup>2</sup>Center for Advanced Genome Engineering, St. Jude Children's Research Hospital, Memphis, Tennessee, USA. <sup>3</sup>Bruker Switzerland AG, Fällanden, Switzerland. <sup>4</sup>Cell and Tissue Imaging Shared Resource, St. Jude Children's Research Hospital, Memphis, Tennessee, USA. <sup>5</sup>Neutron Scattering Division, Oak Ridge National Laboratory, Oak Ridge, TN, USA. <sup>6</sup>Computational Sciences and Engineering Division, Oak Ridge National Laboratory, Oak Ridge, TN, USA. <sup>7</sup>Department of Microbiology, Immunology and Biochemistry, University of Tennessee Health Sciences Center, Memphis, Tennessee, USA. ✉ e-mail: [Richard.Kriwacki@stjude.org](mailto:Richard.Kriwacki@stjude.org)

motifs (R-motifs) in nucleolar proteins, *e.g.*, ribosomal proteins and non-ribosomal proteins<sup>17,18</sup>. Accordingly, purified NPM1 undergoes phase separation with R-motif proteins *in vitro*, forming condensates that mimic the liquid-like features of the nucleolus<sup>16</sup> and interactions with NPM1 facilitate the localization of R-motif proteins to nucleoli<sup>17,19</sup>. Importantly, p14<sup>ARF</sup> contains several multivalent R-motifs, which are required for nucleolar localization and when mutated, as in certain cancers, cause redistribution of p14<sup>ARF</sup> throughout the cell<sup>20,21</sup>.

Many intrinsically disordered proteins, or intrinsically disordered protein regions, adopt compact conformations in isolation under physiological conditions but some assume more expanded conformations after a phase transition<sup>22,23</sup>. Conformational expansion exposes the so-called sticker residues within polypeptide chains to make multivalent interactions that underly intermolecular network formation and phase separation<sup>23</sup>. Crosslinks may also be mediated by folded segments within stretches of otherwise disordered regions. For example, FG nucleoporin hydrogels are scaffolded by intermolecular  $\beta$ -sheet interactions<sup>24</sup>, and TDP43-CTD phase separation requires transient contacts between a conserved  $\alpha$ -helix<sup>25</sup>. We previously showed that p14<sup>ARF</sup> undergoes phase separation with NPM1 *in vitro* and that p14<sup>ARF</sup> restricts NPM1 mobility within condensates<sup>26</sup>.

Here we characterize the structure and dynamics of p14<sup>ARF</sup> and NPM1 within condensates using solution- and solid-state nuclear magnetic resonance (NMR) spectroscopy and small-angle neutron scattering (SANS). We show that p14<sup>ARF</sup> forms meso-scale assemblies within condensates with NPM1, mediated by intermolecular hydrophobic interactions between residues within a partially folded N-terminal region. Further, we show that substitution mutagenesis to abrogate p14<sup>ARF</sup> hydrophobic interactions restores p14<sup>ARF</sup> and NPM1 mobility in condensates while reducing the propensity for phase separation. In nucleoli, p14<sup>ARF</sup> and endogenous NPM1 exhibit reduced diffusion and mobility. Furthermore, p14<sup>ARF</sup> expression reduces cell viability. These phenotypes all correlate with p14<sup>ARF</sup> expression levels and are dependent upon hydrophobic residues within the p14<sup>ARF</sup> N-terminus. These results demonstrate that although the R-motifs are sufficient to induce phase separation with NPM1, the hydrophobicity of p14<sup>ARF</sup> potentiates phase separation and is required for restricting p14<sup>ARF</sup> and NPM1 dynamics within the nucleolus.

## Results

### p14<sup>ARF</sup> forms local and long-range order in NPM1 condensates

Pentameric NPM1 engages its binding partners in part through multivalent electrostatic interactions of its disordered A2 and A3 acidic tracts (Fig. 1A, Supplementary Table 1) and R-motifs in partner proteins<sup>17,18,27–29</sup>. p14<sup>ARF</sup> contains several multivalent R-motifs, termed RI-3 (Fig. 1B, Supplementary Table 1). p14<sup>ARF</sup> also displays three well-conserved N-terminal clusters of hydrophobic residues, termed H1-H3 (Fig. 1B, Supplementary Fig. 1), which are predicted by PSI-PRED4<sup>30</sup> to form  $\alpha$ -helical and  $\beta$ -sheet secondary structures (Fig. 1B; top). Furthermore, the second  $\beta$ -sheet and  $\alpha$ -helix are predicted by ZipperBD<sup>31</sup> to contain amyloidogenic hexapeptide motifs (Fig. 1B; bottom). To gain insight into the structural organization within phase-separated p14<sup>ARF</sup>-NPM1 complexes, we applied contrast variation small-angle neutron scattering (CV-SANS). This approach leverages the differences in the neutron scattering length densities of protons and deuterons to isolate the scattering contributions from select biomolecules in complex mixtures through protein perdeuteration (replacement of H-atoms with D-atoms) and adjustment of the H<sub>2</sub>O/D<sub>2</sub>O ratio within buffers<sup>32</sup>. Fitting the CV-SANS curve of p14<sup>ARF</sup>-NPM1 condensates under p14<sup>ARF</sup>-matched conditions (only scattering from NPM1 detected) to a correlation length model (Fig. 1C, green trace; Supplementary Table 2, see Methods for fitting procedure), yielded a correlation length,  $\xi = 61 \text{ \AA}$ , which is close to the radius of gyration measured in solution,  $R_g = 65 \text{ \AA}$  (Supplementary Fig 2). Within this characteristic length scale,

a scaling exponent describing the NPM1 conformational ensemble was extracted. This factor, from polymer theory, ranges from 0–1, with small values ( $< 0.5$ ) indicative of collapsed or folded conformations, and large values ( $> 0.5$ ) indicative of expanded or unfolded conformations<sup>33</sup>. NPM1 exhibited a scaling exponent,  $\nu = 0.65$ , suggesting that the IDRs of pentameric NPM1<sup>17,18</sup> are in extended conformations in condensates (Fig. 1D). Strikingly, the CV-SANS curves for p14<sup>ARF</sup>-NPM1 condensates under full-scattering conditions (scattering from both NPM1 and p14<sup>ARF</sup> detected) and NPM1-matched conditions (only scattering from p14<sup>ARF</sup> detected) exhibited prominent Bragg peaks (Fig. 1C; gray and blue traces, respectively). The CV-SANS curve from NPM1-matched conditions was fit to a broad peak model, which revealed that p14<sup>ARF</sup> molecules also assume extended conformations ( $\nu = 0.66$ ) and form a meso-scale (100–1000  $\text{\AA}$ ) assembly with a characteristic intermolecular spacing,  $d \approx 180 \text{ \AA}$ , within the condensed phase with NPM1 (Fig. 1C, E). This assembly appears branched at the longest length scales measured ( $\nu = 0.35$ ) with an inter-contact distance<sup>34</sup>,  $\Xi \approx 160 \text{ \AA}$  (Fig. 1C, E; magenta contacts). Meso-scale ordering of this type is common within phase separated materials, *e.g.*, polymer gels, and is caused by physical crosslinks<sup>32</sup>.

We next characterized the residue-level structure of p14<sup>ARF</sup> within condensates with NPM1 and identified sites of intra- and intermolecular p14<sup>ARF</sup> contacts using NMR spectroscopy. The two-dimensional transverse relaxation-optimized spectroscopy, heteronuclear single-quantum <sup>1</sup>H-<sup>15</sup>N correlation (2D <sup>1</sup>H-<sup>15</sup>N TROSY-HSQC) spectrum of [<sup>13</sup>C,<sup>15</sup>N]-p14<sup>ARF</sup> within condensates with unlabeled NPM1 revealed resonances for a subset of residues (Supplementary Fig. 3). Using triple-resonance NMR methods (see Methods), these were assigned to residues in the C-terminal region of p14<sup>ARF</sup>, following R-motif R3 (Supplementary Fig. 4, Supplementary Table 3, Supplementary Table 4), indicating that this region of p14<sup>ARF</sup> is disordered in condensates with NPM1. In contrast, N-terminal p14<sup>ARF</sup> residues showed extensive resonance broadening and could not be analyzed using solution-state NMR methods.

We reasoned that resonance broadening resulted from limited mobility of p14<sup>ARF</sup> within its phase separated meso-scale assemblies, as indicated by previous fluorescence recovery after photobleaching (FRAP) results<sup>26</sup>. Therefore, we applied cross-polarization magic-angle spinning solid-state NMR (CP-MAS ssNMR) (see Methods; Supplementary Table 5), which can detect resonances for both mobile (Supplementary Fig. 5) and immobile (Fig. 1F) segments of proteins within condensates<sup>26</sup>. Analysis of multiple two- and three-dimensional ssNMR spectra enabled resonance assignments for residues within the p14<sup>ARF</sup> N-terminus (Supplementary Figs. 6, 7; Supplementary Table 6). Analysis of secondary <sup>13</sup>C chemical shifts, which report on secondary structure, revealed that the N-terminal portion of p14<sup>ARF</sup> adopts  $\alpha$ -helical and  $\beta$ -strand secondary structure in condensates with NPM1 (Fig. 1G).

Consistent with the findings from CV-SANS, in 2D <sup>13</sup>C-<sup>13</sup>C dipolar assisted rotational resonance (CC-DARR) spectra, we observed only one long-range intramolecular contact in p14<sup>ARF</sup>, between T8 and H26, which was most evident at DARR mixing times above 200 ms (Fig. 2A, B; Supplementary Fig. 6C, D). These findings suggest that compact conformations are not highly populated or form only transiently. To probe for intermolecular p14<sup>ARF</sup>-p14<sup>ARF</sup> contacts, we recorded NHHN spectra<sup>35</sup> for a p14<sup>ARF</sup>-NPM1 condensate comprised of a 1:1 mixture of independently <sup>15</sup>N- or <sup>13</sup>C-labeled p14<sup>ARF</sup> molecules, to ensure that only intermolecular <sup>15</sup>N-<sup>13</sup>C correlations were detected<sup>36</sup>. The resulting spectrum showed a high degree of similarity to 2D HNCA and 2D HNCACX spectra, demonstrating that structured regions within the p14<sup>ARF</sup> N-terminus engage in intermolecular contacts (Fig. 2C, D). Furthermore, based on the low signal-to-noise ratio observed, persistent p14<sup>ARF</sup> contacts either constitute a minor state or occur over long distances.

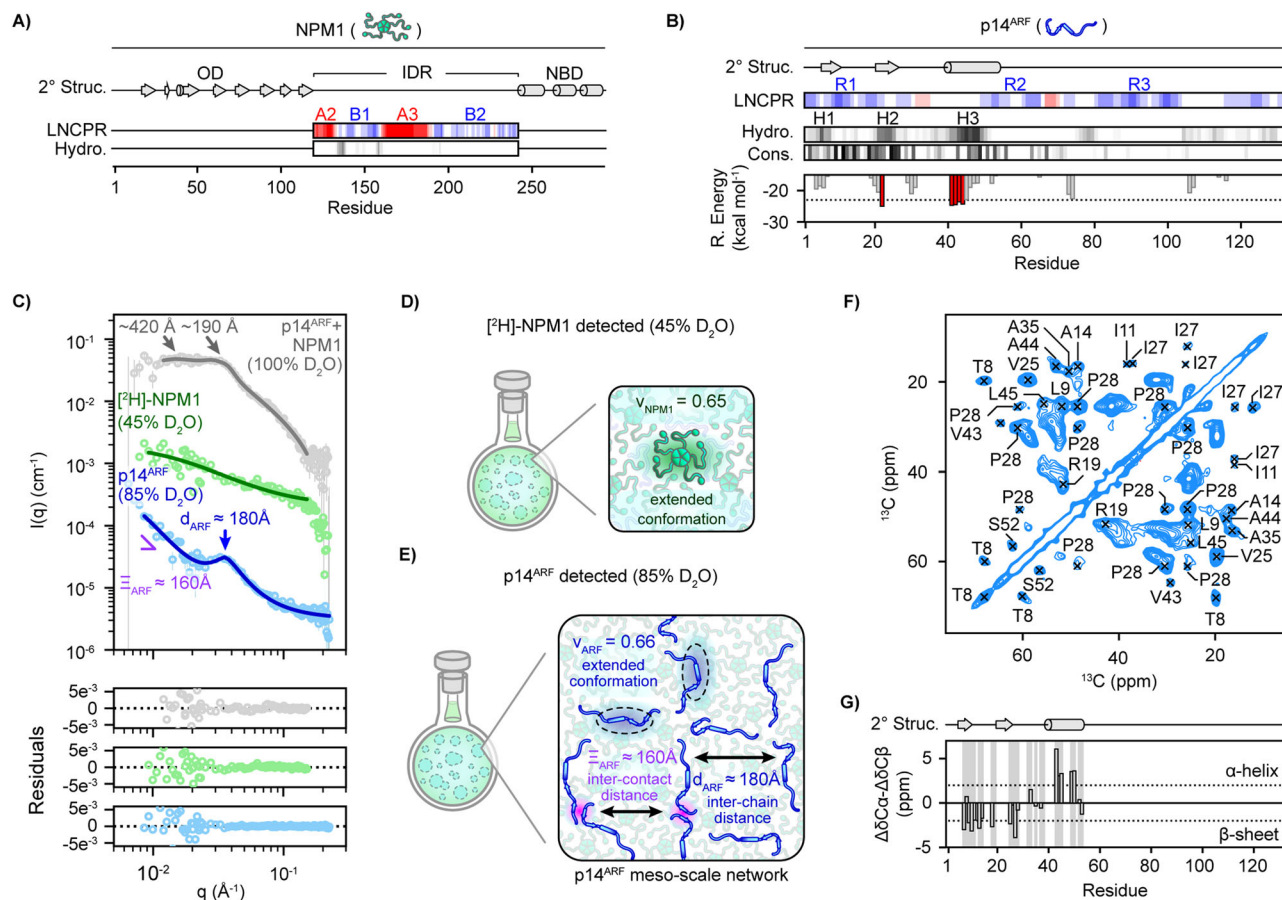


**Fig. 1 | p14<sup>ARF</sup> exhibits local and long-range ordering within condensates with NPM1.** **A** NPM1 structural features, including the secondary structure calculated from the oligomerization domain (OD) PDB 4NSM and the nucleic acid binding domain (NBD) PDB 2LLH, using DSSP (2° Struc.;  $\beta$ -strands are indicated with arrows and  $\alpha$ -helices are indicated with cylinders). The CIDER linear net charge per residue (LNCPR) and linear hydrophathy (Hydro.) are shown for the IDR. **B** p14<sup>ARF</sup> structural features, including PSI-PRED secondary structure prediction (2° Struc.), CIDER linear net charge per residue (LNCPR), and linear hydrophathy (Hydro.). The amino acid sequence conservation (Cons.) is based on a multiple sequence alignment using MUSCLE. The bottom panel shows the Rosetta steric zipper propensity energy (R. Energy) calculated using ZipperDB. **C** CV-SANS curves for p14<sup>ARF</sup>-NPM1 condensates, in 100% D<sub>2</sub>O buffer for full scattering intensity (NPM1 and p14<sup>ARF</sup> detected; gray trace), in 45% D<sub>2</sub>O buffer where p14<sup>ARF</sup> is contrast matched ([<sup>2</sup>H]-[<sup>2</sup>H]-NPM1 detected; green trace), and in 85% D<sub>2</sub>O buffer where [<sup>2</sup>H]-NPM1 is contrast matched (p14<sup>ARF</sup> detected; blue trace). Correlation peaks at ~200 Å and ~400 Å correspond to meso-scale organization of p14<sup>ARF</sup>. All curves are offset for clarity. Scatter points represent the average, the error bars represent the uncertainty derived from the counting statistics of the SANS instrument, as described and cited in the Methods. **D** Schematic describing NPM1 with extended IDR conformations. **E** Schematic describing the spatial organization of p14<sup>ARF</sup> within p14<sup>ARF</sup>-NPM1 condensates. **F** 2D CC-DARR spectrum of [<sup>13</sup>C,<sup>15</sup>N]-p14<sup>ARF</sup> within the condensed phase. Select resonance assignments are labeled. **G** Secondary <sup>13</sup>C chemical shifts for [<sup>13</sup>C,<sup>15</sup>N]-p14<sup>ARF</sup> within the condensed phase. Assigned residues are highlighted in gray. The secondary structure prediction for panel B is shown for reference (2° Struc.; top).

### NPM1's IDR is disordered in the condensed phase with p14<sup>ARF</sup>

We previously applied CP-MAS ssNMR to show that the N-terminal NPM1 oligomerization domain (OD) retains secondary structure in condensates with p14<sup>ARF</sup> and experiences limited mobility<sup>26</sup>. However, we detected no resonances corresponding to residues in the NPM1 central IDR or the C-terminal, nucleic acid binding domain (NBD), suggesting that these structural elements remain dynamic. Therefore, we applied solution-state NMR to probe the structure and dynamics of the NPM1 IDR within p14<sup>ARF</sup>-NPM1 condensates. The 2D <sup>1</sup>H-<sup>15</sup>N TROSY-HSQC spectrum for condensed [<sup>13</sup>C, <sup>15</sup>N]-NPM1 showed resonances for residues in the IDR, although resonance broadening was apparent (Fig. 3A). This stemmed from an enhancement in <sup>15</sup>N R<sub>2</sub> relaxation, as detected through measurements of different types of nuclear spin relaxation (Fig. 3B–E). This was most pronounced for residues closest to the A3 acidic tract (residues 161–188), which mediates interactions with R-motif-containing proteins<sup>19</sup>, including Arf<sup>2</sup>. Interestingly, a portion of the R<sub>2</sub> enhancement was caused by chemical exchange as measured by <sup>15</sup>N Carr-Purcell-Meiboom-Gill (<sup>15</sup>N-CPMG) relaxation dispersion (Fig. 3F, G). Fitting to a 2-state exchange model showed that

interconversion of NPM1 IDR conformations occurred on the 100 s of  $\mu$ s timescale (Fig. 3G, Supplementary Fig. 8, Supplementary Table 7, see Methods). This suggests that the condensate environment restrains the conformational dynamics of the NPM1 IDR (Fig. 3H).

interconversion of NPM1 IDR conformations occurred on the 100 s of  $\mu$ s timescale (Fig. 3G, Supplementary Fig. 8, Supplementary Table 7, see Methods). This suggests that the condensate environment restrains the conformational dynamics of the NPM1 IDR (Fig. 3H).

### p14<sup>ARF</sup> hydrophobic residues limit condensed NPM1's mobility

We hypothesized that the hydrophobic interfaces in the p14<sup>ARF</sup> N-terminal region are involved in interactions that drive phase separation and reduce NPM1 mobility within condensates. To test this, we substituted multiple aliphatic residues (Ile, Leu, and Val) within the p14<sup>ARF</sup> N-terminus with Gly and Ser (termed p14<sup>ARF</sup> $\Delta$ H1-3) (Fig. 4A, Supplementary Table 1). We then performed titrations of p14<sup>ARF</sup> and p14<sup>ARF</sup> $\Delta$ H1-3 into solutions of Alexa Fluor 488 conjugated NPM1 (NPM1-AF488) and determined their respective thresholds for heterotypic phase separation (termed saturation concentration values, C<sub>sat</sub>) using confocal fluorescence microscopy (Fig. 4B–D). As expected, the C<sub>sat</sub> value for phase separation of p14<sup>ARF</sup> $\Delta$ H1-3 with NPM1-AF488 was greater than that for p14<sup>ARF</sup> (Fig. 4C, D). The free energy of transfer for NPM1,  $\Delta G_{\text{NPM1}}^{\text{tr}}$ , which reports on the thermodynamics of partitioning



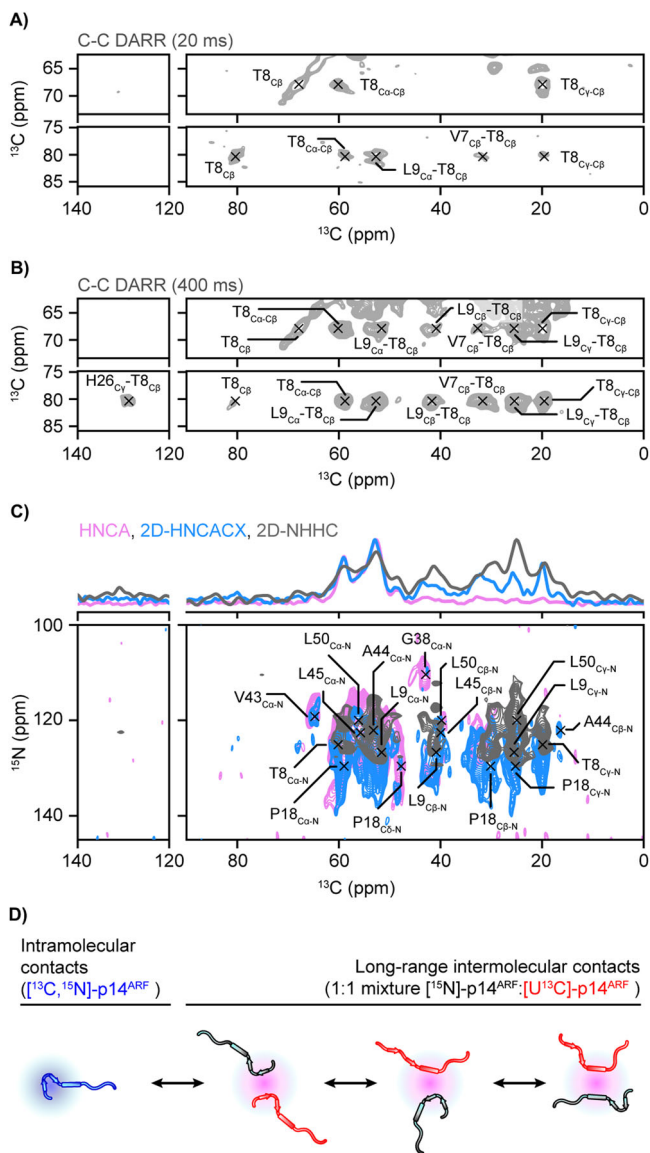


**Fig. 2 | p14<sup>ARF</sup> engages in intra- and intermolecular contacts within the condensed phase with NPM1.** **A** A C-C DARR spectrum acquired for [<sup>13</sup>C,<sup>15</sup>N]-p14<sup>ARF</sup> with 20 ms DARR mixing time shows resonances for T8 in two states, including in an expanded p14<sup>ARF</sup> conformation (top), and in a collapsed p14<sup>ARF</sup> conformation (bottom). **B** A C-C DARR spectrum acquired with 400 ms DARR mixing time shows additional cross-peaks indicating intramolecular contacts between T8 and H26. **C** The 2D-NHHC spectrum (gray) of p14<sup>ARF</sup> (equal mixture of [<sup>13</sup>C]-p14<sup>ARF</sup> and [<sup>15</sup>N]-p14<sup>ARF</sup>) shows that sidechains within the p14<sup>ARF</sup> N-terminus make intermolecular contacts within the condensed phase with NPM1. HNCA (magenta) and 2D-HNCACX (blue) spectra for [<sup>13</sup>C,<sup>15</sup>N]-p14<sup>ARF</sup> are shown for reference. **D** Schematic describing possible modes of p14<sup>ARF</sup> intra- and intermolecular interaction.

from the light to the dense phase<sup>37</sup>, were markedly lower across the p14<sup>ARF</sup> titration as compared to the p14<sup>ARF</sup>ΔH1-3 titration, demonstrating that p14<sup>ARF</sup> hydrophobic residues enhance the propensity for NPM1 phase separation (Fig. 4D). Interestingly, for titration points above a 1:1 molar ratio, p14<sup>ARF</sup> increased the  $\Delta C_{IT}^{NPM1}$ , demonstrating that NPM1 becomes destabilized within the condensate network at saturating p14<sup>ARF</sup> concentrations (Fig. 4C, D). This transition mirrored the reentrant phase behavior observed for other Arg-rich proteins in condensates with NPM1<sup>19</sup>.

CV-SANS analysis of p14<sup>ARF</sup>ΔH1-3-NPM1 condensates showed that substitution of the hydrophobic residues in p14<sup>ARF</sup> abrogates meso-

scale ordering of p14<sup>ARF</sup> molecules within the condensed phase with NPM1 (Fig. 4E). The NPM1 IDRs were in extended conformations, as in condensates with p14<sup>ARF</sup> (Fig. 4F). However, p14<sup>ARF</sup>ΔH1-3 molecules appeared slightly more expanded as compared to p14<sup>ARF</sup>, with a scaling exponent,  $\nu = 0.82$  (Fig. 4G), likely due to an increase in structural disorder.

To test whether the elimination of p14<sup>ARF</sup> hydrophobic interfaces would enhance NPM1 mobility within condensates, we performed FRAP assays on p14<sup>ARF</sup>-NPM1-AF488 and p14<sup>ARF</sup>ΔH1-3-NPM1-AF488 condensates (Fig. 4H–J; Supplementary Fig. 9,10). Within condensates containing p14<sup>ARF</sup>ΔH1-3, NPM1-AF488 exhibited significantly greater mobility (Fig. 4I) and faster diffusion (based on apparent diffusion rates,  $D_{App}$ ) (Fig. 4J) as compared to condensates containing p14<sup>ARF</sup>. Taken together, these results show that hydrophobic residues within the p14<sup>ARF</sup> N-terminus act as stickers<sup>23</sup> that mediate self-association, enhance multivalent heterotypic interactions that drive phase separation with NPM1, and promote the meso-scale assembly of p14<sup>ARF</sup> molecules, thus restricting NPM1 translational diffusion.

### p14<sup>ARF</sup> reduces nucleolar NPM1 mobility and cell proliferation

NPM1 localizes p14<sup>ARF</sup> in nucleoli to inhibit it from engaging other binding partners and activating anti-proliferative pathways<sup>4</sup>. Given that NPM1 usually forms dynamic, liquid-like condensates<sup>27</sup> and in the absence of denaturants, purified p14<sup>ARF</sup> rapidly precipitates from solution<sup>38</sup>, we reasoned that p14<sup>ARF</sup> and NPM1 form condensates that block p14<sup>ARF</sup> aggregation by capturing it within the gel-like interaction network of the meso-scale assembly. This is akin to NPM1's role as a chaperone for misfolded proteins in the nucleolus during cellular stress<sup>39</sup>. On the other hand, overexpression of p19<sup>Arf</sup> promotes NPM1 degradation<sup>13</sup> and the assembly of high molecular weight p19<sup>Arf</sup>-containing complexes<sup>2</sup>. Based on these observations, we reasoned that an abundance of NPM1 is needed to form stable p14<sup>ARF</sup>-NPM1 complexes in nucleoli and limit the potential for p14<sup>ARF</sup> homo- and heterooligomerization with other nucleolar biomacromolecules. Therefore, we next asked whether expression of p14<sup>ARF</sup> alters the dynamics of NPM1 in nucleoli.

We addressed this question using the human DLD-1 colorectal adenocarcinoma cell line, which harbors transcriptionally inactive, mutant p53 (p53<sup>S241F</sup>)<sup>40,41</sup> and is effectively p14<sup>ARF</sup>-null due to promotor hypermethylation<sup>42</sup>. We performed CRISPR-Cas9 editing to insert the gene for monomeric, enhanced green fluorescent protein (mEGFP)<sup>43</sup> at the 3'-end of both alleles of the NPM1 gene, leading to expression of C-terminally mEGFP-tagged NPM1 at endogenous levels (NPM1-GFP; Supplementary Table 1), termed DLD-1<sup>NPM1-G</sup> cells. Next, we performed lentiviral transduction of DLD-1<sup>NPM1-G</sup> cells to enable doxycycline-inducible expression of p14<sup>ARF</sup> fused at the C-terminus to the monomeric, near-infrared fluorescent protein, miRFP670 (p14<sup>ARF</sup>-iRFP; Supplementary Table 1)<sup>44</sup>. As expected, following doxycycline induction, p14<sup>ARF</sup>-iRFP localized to nucleoli with NPM1-GFP (Fig. 5A). High-throughput imaging of DLD-1<sup>NPM1-G</sup> nucleoli showed that nucleolar NPM1-GFP and p14<sup>ARF</sup>-iRFP levels were anti-correlated (Fig. 5B; Supplementary Figs. 11 and 12A, B).

We next performed FRAP of p14<sup>ARF</sup>-iRFP and NPM1-GFP in DLD-1<sup>NPM1-G</sup> cells (Supplementary Figs. 9, and 12C–E). Consistent with our in vitro results, we observed a substantial reduction in  $D_{App}$  and mobility values for NPM1-GFP with increasing p14<sup>ARF</sup>-iRFP levels (Supplementary Fig. 13A–G). Similarly,  $D_{App}$  and mobility values for p14<sup>ARF</sup>-iRFP itself decreased as its levels increased (Supplementary Fig. 13H,I). To assess the dependence of this effect on the level of p14<sup>ARF</sup>-iRFP expression, we first used flow cytometry to isolate DLD-1<sup>NPM1-G</sup> clones that expressed p14<sup>ARF</sup>-iRFP at different levels (Supplementary Fig. 14A). Consistent with our observations with unsorted DLD-1<sup>NPM1-G</sup> cells, expression of p14<sup>ARF</sup>-iRFP in the isolated DLD-1<sup>NPM1-G</sup> clones caused dose-dependent reductions in  $D_{App}$  and mobility for NPM1-GFP, which was correlated with values for p14<sup>ARF</sup>-iRFP (Fig. 5C–E, Supplementary Fig. 14B,C). We

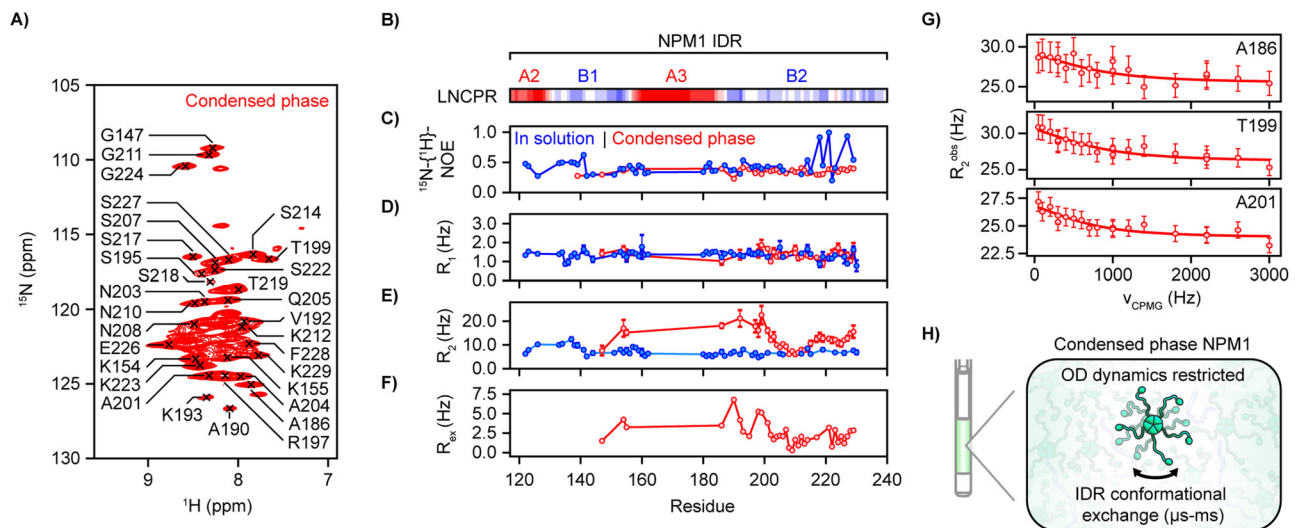


**Fig. 3 | The NPM1 IDR retains disorder and experiences attenuated backbone motions within the condensed phase with p14<sup>ARF</sup>.** **A** The 2D <sup>1</sup>H-<sup>15</sup>N TROSY-HSQC spectrum of [<sup>13</sup>C,<sup>15</sup>N]-NPM1 within the p14<sup>ARF</sup>-NPM1 condensed phase displays resonances from the NPM1 IDR. **B** Linear net charge per residue (LNCPR) for the NPM1 IDR. Nuclear spin relaxation for [<sup>2</sup>H,<sup>15</sup>N]-NPM1 in solution (blue scatter points) and condensed phase [<sup>13</sup>C,<sup>15</sup>N]-NPM1 (red scatter points), including **C** <sup>1</sup>H-<sup>15</sup>N heteronuclear NOEs, **D**  $R_1$ , and **E**  $R_2$  transverse relaxation, which shows a restriction of NPM1 IDR backbone motions on the ps-ns timescale. The error bars for  $R_1$  and  $R_2$

transverse relaxation plots represent the standard errors from curve fitting, as described in Methods. **F** The contributions from exchange broadening,  $R_{ex}$ . **G** <sup>15</sup>N-CPMG relaxation dispersion profiles for condensed [<sup>13</sup>C,<sup>15</sup>N]-NPM1 measured at 800 MHz, including A186, T199, and A201, fit to a two-state model. Scatter points represent the decay rates, and the error bars represent the estimated systematic error, as described in Methods. **H** Schematic describing NPM1 IDR conformational exchange within condensates with p14<sup>ARF</sup>.

then monitored p14<sup>ARF</sup>-iRFP and NPM1-GFP diffusion for two clones (termed G2 and B11) before, 24 h, and 48 h after doxycycline induction of p14<sup>ARF</sup>-iRFP expression. Both DLD-1<sup>NPM1-G</sup> clones showed significant reductions in the  $D_{App}$  value for p14<sup>ARF</sup>-iRFP and NPM1-GFP within 24 h, which persisted after 48 h of p14<sup>ARF</sup>-iRFP expression (Supplementary Fig. 14D,E). Furthermore, NPM1-GFP mobility was reduced in both DLD-1<sup>NPM1-G</sup> cell clones at the 48-hour time point (Supplementary Fig. 14F,G). Consistent with previous reports of p14<sup>ARF</sup> expression in p53-null cell lines<sup>6,45</sup>, expression of p14<sup>ARF</sup>-iRFP correlated with reduced viability of DLD-1<sup>NPM1-G</sup> cells in a dose- and time-dependent manner (Supplementary Fig. 13H,I).

We hypothesized that the reductions in diffusion for p14<sup>ARF</sup>-iRFP and NPM1-GFP are dependent on hydrophobic residues within p14<sup>ARF</sup>'s N-terminal  $\beta$ -strands and  $\alpha$ -helix and tested this by expressing miRFP670-tagged p14<sup>ARF</sup> $\Delta$ HI-3 (p14<sup>ARF</sup> $\Delta$ HI-3-iRFP) in DLD-1<sup>NPM1-G</sup> cells (Supplementary Fig. 15A). Using high-throughput imaging, we did not observe a reduction in nucleolar NPM1 levels with increasing p14<sup>ARF</sup> $\Delta$ HI-3-iRFP levels (Supplementary Fig. 15B,C). We next performed FRAP of p14<sup>ARF</sup> $\Delta$ HI-3-iRFP and NPM1-GFP in DLD-1<sup>NPM1-G</sup> cells and observed no apparent reduction in diffusion rate or mobility for p14<sup>ARF</sup> $\Delta$ HI-3-iRFP or NPM1-GFP with increasing p14<sup>ARF</sup> $\Delta$ HI-3-iRFP levels (Supplementary Fig. 15D,E). We further used single-cell sorting to identify DLD-1<sup>NPM1-G</sup> clones that expressed p14<sup>ARF</sup> $\Delta$ HI-3-iRFP at varied levels (Supplementary Fig. 15F). We next performed FRAP assays to monitor p14<sup>ARF</sup> $\Delta$ HI-3-iRFP and NPM1-GFP diffusion over the course of two days, for clones C10 and H5, which expressed p14<sup>ARF</sup> $\Delta$ HI-3-iRFP levels comparable to p14<sup>ARF</sup>-iRFP in clones G2 and B11. In contrast to results with wild-type p14<sup>ARF</sup>-iRFP, for clones C10 and H5,  $D_{App}$  values for NPM1-GFP remained relatively constant after induced expression of p14<sup>ARF</sup> $\Delta$ HI-3-iRFP (Supplementary Fig. 15G,H), reduced NPM1-GFP mobility was not observed (Supplementary Fig. 14I,J), and importantly, cell proliferation was not significantly reduced (Supplementary Fig. 15K,L). Indeed, during enforced expression of p14<sup>ARF</sup> $\Delta$ HI-3-iRFP, DLD-1<sup>NPM1-G</sup> cells proliferated to the same extent as during expression of miRFP670 (iRFP) alone (Supplementary Fig. 15M). However, nucleolar partitioning of p14<sup>ARF</sup> $\Delta$ HI-3-iRFP was reduced relative to that of p14<sup>ARF</sup>-

iRFP (Supplementary Fig. 15N). Thus, in agreement with our observations of in vitro p14<sup>ARF</sup>-NPM1 condensates, hydrophobic residues within the p14<sup>ARF</sup> N-terminus enhance nucleolar partitioning and mediate interactions in nucleoli that restrain p14<sup>ARF</sup>-iRFP and NPM1-GFP dynamics (Fig. 5F).

## Discussion

The thermodynamics of multicomponent phase separation dictates that an expansion in the number of biomolecular interaction modes within a system can give rise to high-dimensional phase behavior<sup>37,46</sup>. The partitioning of an individual component is governed by its net interaction strength, and can be modulated by its concentration and those of other components of the condensate network<sup>37</sup>. For the p14<sup>ARF</sup>-NPM1 phase transition, heterotypic interactions (p14<sup>ARF</sup>-NPM1) and p14<sup>ARF</sup> homotypic interactions, mediated by N-terminal hydrophobic residues, drive phase separation. Accordingly, the p14<sup>ARF</sup> $\Delta$ HI-3-NPM1 phase transition was characterized by an increased  $C_{sat}$  and  $\Delta G^{\ddagger}$  for NPM1. The introduction of competitive homotypic interactions, *i.e.*, p14<sup>ARF</sup> homotypic interactions which are stronger than heterotypic interactions with NPM1, creates a mechanism whereby NPM1 partitioning can be modulated by p14<sup>ARF</sup>. By tuning the condensed phase p14<sup>ARF</sup> composition such that p14<sup>ARF</sup> homotypic interactions exceed heterotypic interactions with NPM1, the NPM1 component becomes destabilized. This was observed for in vitro condensates, where additions of p14<sup>ARF</sup> to NPM1 above a 1:1 molar ratio increased the NPM1  $\Delta G^{\ddagger}$ .

We previously showed that the diffusion of NPM1 within condensates containing p14<sup>ARF</sup> is characteristically slow and a large population of NPM1 molecules are immobile. This immobile form of NPM1 constitutes one of the two components of the p14<sup>ARF</sup>-NPM1 condensate network<sup>26</sup>, with hydrophobic p14<sup>ARF</sup> constituting the other. For the NPM1 component, using CV-SANS, we found that the orientation of the NPM1 molecules within the condensed phase is disordered and NPM1 IDRs assume expanded conformations within a characteristic correlation length, which is close to the radius of gyration in solution. Further, using NMR, we showed that the NPM1 IDR is also





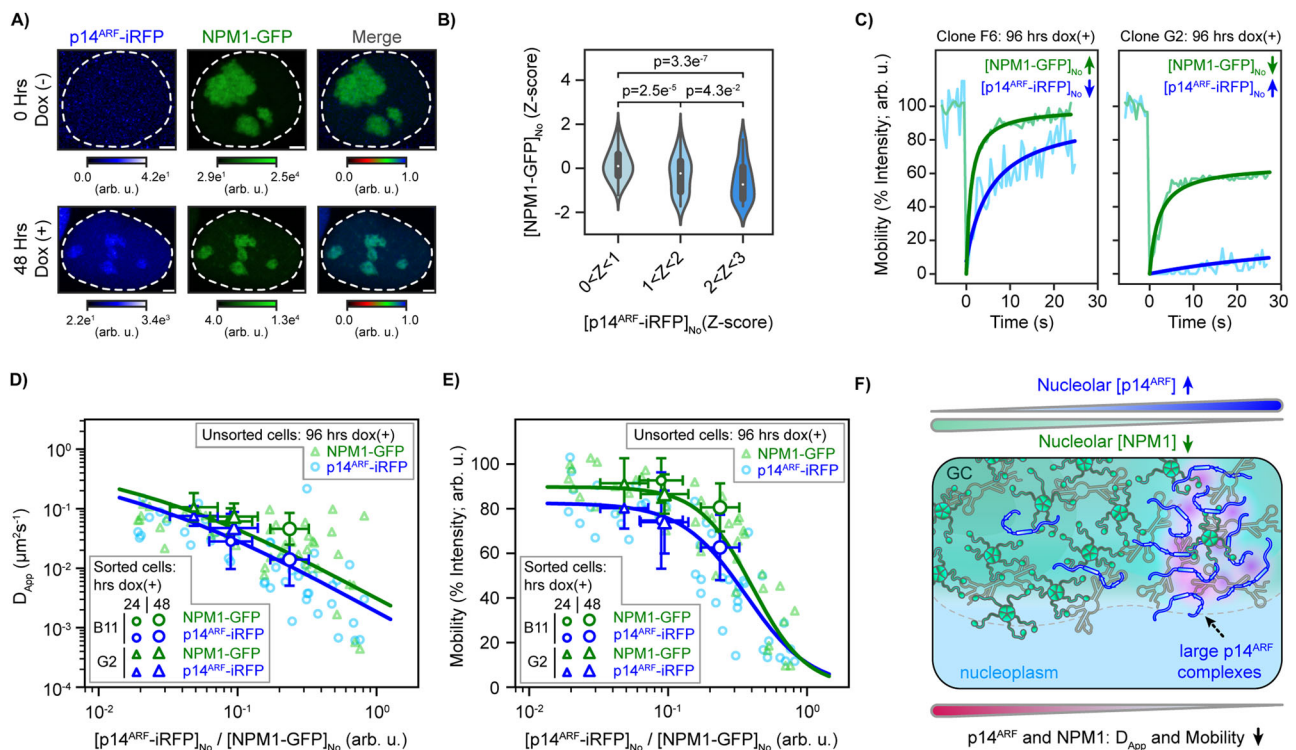


**Fig. 5 | p14<sup>ARF</sup> reduces nucleolar NPM1 diffusion in a concentration dependent manner.** **A** Zoomed-in regions from fluorescence microscopy images of live DLD-1<sup>NPM1-G</sup> (clone B11) cells, before and after 48 h of doxycycline induced p14<sup>ARF</sup>-iRFP expression. Scale bars = 2 μm. **B** Z-score analysis of NPM1-GFP and p14<sup>ARF</sup>-iRFP levels in DLD-1<sup>NPM1-G</sup> cells, showing that p14<sup>ARF</sup> and NPM1 levels are anti-correlated (statistical significance was assessed by two-sided Mann-Whitney U-test,  $n = 2272, 122, 54$  cells,  $p$ -values are shown in the figure). **C** FRAP curves with fits, as described in Methods, for cells sorted from the DLD-1<sup>NPM1-G</sup> population shown in B. The curves on the left are from a cell expressing a high level of nucleolar NPM1 (clone F6; green trace) and a low level of nucleolar p14<sup>ARF</sup> (clone F6; blue trace). The curves on the

right are from a cell expressing a low level of nucleolar NPM1 (clone G2; green trace) and a high level of nucleolar p14<sup>ARF</sup> (clone G2; blue traces). In unsorted DLD-1<sup>NPM1-G</sup> cells, **D** The  $D_{app}$  and **E** mobility for nucleolar NPM1-GFP and p14<sup>ARF</sup>-iRFP (small green and blue transparent markers, respectively,  $n = 45$  cells) are reduced as nucleolar p14<sup>ARF</sup>-iRFP levels increase. Reductions also occur as the duration of p14<sup>ARF</sup>-iRFP expression is extended (large opaque markers; scatter points represent the mean and error bars represent the standard deviation, where  $n = 20$  cells). **F** A schematic describing the correlated reductions in p14<sup>ARF</sup> and NPM1 dynamics and their assembly into large molecular weight complexes within the granular component (GC) of the nucleolus.

the ssNMR timescale, in slow exchange between a large population of expanded conformations and a small population of collapsed conformations. Using CV-SANS we found that the bulk of p14<sup>ARF</sup> assumes expanded conformations that are ordered into meso-scale assemblies. This structural organization results from the p14<sup>ARF</sup> homotypic interaction network, as evidenced by the lack of long-range ordering within p14<sup>ARF</sup> ΔH1-3-NPM1 condensates and provides a basis for the characteristically slow diffusion measured for condensed phase p14<sup>ARF</sup> and NPM1<sup>26</sup>.

In DLD-1<sup>NPM1-G</sup> nucleoli, the apparent concentrations of p14<sup>ARF</sup> and NPM1 were anti-correlated, with significantly reduced NPM1 levels observed at elevated p14<sup>ARF</sup> levels, suggesting that p14<sup>ARF</sup> has a destabilizing effect on NPM1's heterotypic interactions in nucleoli. For example, p14<sup>ARF</sup> may induce reentrant phase behavior in the GC, like Arg-rich di-peptide repeat proteins (DPRs), which induce dissolution of nucleoli<sup>19</sup>. This trend was not observed for p14<sup>ARF</sup> ΔH1-3 and partitioning of p14<sup>ARF</sup> ΔH1-3 into DLD-1<sup>NPM1-G</sup> nucleoli was significantly lower than for wild type p14<sup>ARF</sup>. Furthermore, NPM1 and p14<sup>ARF</sup> experienced significantly reduced diffusion at elevated nucleolar p14<sup>ARF</sup> levels. Taken together, hydrophobic interactions enhance partitioning of p14<sup>ARF</sup> into nucleoli and drive the assembly of large, slowly diffusing complexes containing NPM1. Importantly, p14<sup>ARF</sup> intoxicates DLD-1<sup>NPM1-G</sup> cells as its levels rise, consistent with its tumor suppressor activity in response to oncogene activation<sup>1</sup>. This toxicity may stem from reduced NPM1 levels or mobility, which may impair NPM1 nucleolar function, e.g., ribosomal subunit maturation and export<sup>48</sup>. In addition, p14<sup>ARF</sup> may

engage other nucleolar biomolecules, e.g. ribosomal proteins or rRNA<sup>2,49</sup>. Conserved hydrophobic and Arg-rich motifs within the N-termini of p14<sup>ARF</sup> and p19<sup>Arf</sup> (termed Arf-motifs<sup>14</sup>) are required for p19<sup>Arf</sup> dependent pre-rRNA processing defects<sup>45</sup>. Arf-motifs are also required for binding the central acidic IDR of HDM2, and localizing HDM2 to nucleoli<sup>14</sup>. Interestingly, Arf-motif peptides form soluble, β-strand-rich structures upon binding cognate acidic motifs in HDM2<sup>14,50–52</sup>. Adoption of secondary structure within Arf may thus be a common mechanism underlying its interactions with acid-tract-containing, protein binding partners.

## Methods

### Cell lines

The following cell lines were purchased from American Type Culture Collection (ATCC): DLD-1 (male, adult, age not reported, Duker's type C colon cancer), DLD-1 cells were cultured in RPMI 1640 medium (ThermoFisher) supplemented with 10% fetal bovine serum and 100 U/mL penicillin/streptomycin. The DLD-1 cells harboring doxycycline-inducible p14<sup>ARF</sup>-miRFP670, p14<sup>ARF</sup> ΔH1-3-miRFP670, miRFP670, were maintained in RPMI 1640 medium supplemented with 10% Tet system approved fetal bovine serum (ThermoFisher), and 250 μg/ml G418. All cell lines were incubated at 37 °C in a humidified incubator with 5% CO<sub>2</sub>. Gene edited cell lines were authenticated by short tandem repeat (STR) profiling. Cells were tested negative for mycoplasma by the e-Myco PLUS Mycoplasma PCR Detection Kit (BullDog Bio).

## Escherichia coli strains

*Escherichia coli* BL21(DE3) cells were used to produce recombinant proteins. NEB Stable Competent *Escherichia coli* cells (New England Biolabs) were used when subcloning genes into lentiviral vectors. All other vectors were transformed to DH5 $\alpha$  competent cells (taxid: 668369). The NEB Stable cells and the other *E. coli* strains were grown at 30 °C and 37 °C, respectively.

## Plasmid and cloning methods

For *E. Coli* expression of the recombinant proteins including NPM1 and wild-type p14<sup>ARF</sup>, their DNA coding sequences were subcloned to the pET-28a(+) plasmid (EMD Biosciences) as previously described<sup>18,26</sup>. The DNA sequence encoding the p14<sup>ARF</sup>  $\Delta$ H1-3 mutant was de novo synthesized as gBlocks (Integrated DNA Technologies) and subcloned into pET-28a(+) using the BamHI and HindIII sites. The protein sequence of the p14<sup>ARF</sup>  $\Delta$ H1-3 mutant is provided in Supplementary Table 1. To express proteins tagged with the monomeric, near-infrared fluorescent protein, mRFP670<sup>44</sup>, we synthesized the cDNAs of mRFP670, and p14<sup>ARF</sup> or p14<sup>ARF</sup>  $\Delta$ H1-3 C-terminally fused with mRFP670 following a (GGG)<sub>5</sub> linker. These were subcloned into the NheI and Sall restriction sites of the pCDH-PGK vector, a gift from Kazuhiro Oka (Addgene plasmid # 72268; <http://n2t.net/addgene:72268>; RRID: Addgene\_72268). The protein sequences of these constructs are provided in Supplementary Table 1. The coding regions were then PCR-amplified with a common pair of primers (forward: 5'-CACCATCTGCACGCTTCAAAG-3'; reverse: 5'-CCACATAGCGTAAAGGAGCAAC-3'). The PCR products were subsequently TOPO cloned into the pENTR vector using the pENTR/SD/D-TOPO Cloning Kit (ThermoFisher). All plasmid constructs were verified with DNA sequencing performed by Hartwell Center DNA Sequencing Core at St. Jude Children's Research Hospital and by Massachusetts General Hospital CCIB DNA core.

## Expression and purification of recombinant proteins

Recombinant poly-histidine-tagged NPM1 in pET28a (+) (Novagen) were expressed in BL21 (DE3) *Escherichia coli* cells (Millipore Sigma, Burlington, MA, USA) grown at 37 °C in LB medium supplemented with 30  $\mu$ g/ml of Kanamycin. For isotopic labeling to generate [<sup>13</sup>C,<sup>15</sup>N]-NPM1, cells were grown in MOPS-based minimal media containing [<sup>13</sup>C<sub>6</sub>]-D-glucose and <sup>15</sup>NH<sub>4</sub>Cl (Cambridge Isotope Laboratories)<sup>53</sup>. At OD<sub>600nm</sub> = 0.8, 0.5 mM Isopropyl  $\beta$ -D-1 thiogalactopyranoside (IPTG) was added, cells were incubated at 37 °C for an additional 3 h and harvested by centrifugation at 3800  $\times$  g at 4 °C. NPM1 was purified from the soluble lysate fraction using Ni-NTA affinity chromatography. Affinity tags were removed via proteolytic cleavage with tobacco etch virus (TEV) protease and purified using a C<sub>4</sub> HPLC (Higgins Analytical, Mountain View, CA, USA) with a H<sub>2</sub>O/CH<sub>3</sub>CN/0.1% trifluoroacetic acid solvent system. NPM1 constructs were refolded by resuspending lyophilized protein in 6 M guanidine HCl and dialyzing against 10 mM Tris, 150 mM NaCl, 2 mM dithiothreitol (DTT), pH 7.5 buffer. Aliquots of NPM1 constructs were flash frozen and stored at -80 °C. For the production of [<sup>2</sup>H]-NPM1 used in SANS studies, cells were cultured in Enfor's minimal media<sup>54</sup> with 70% D<sub>2</sub>O (Cambridge Isotope Laboratories), yielding a 52% deuteration level<sup>19</sup>. Preparation of Alexa Fluor 488 conjugated NPM1 was performed as described<sup>27</sup>. Briefly, Alexa Fluor 488 (Thermo Fisher Scientific, Waltham, MA, USA) was conjugated to NPM1 at Cys104 (NPM1-AF488) following the manufacturer's protocol. To generate NPM1 pentamers labeled at a single subunit, fluorescently labeled NPM1-AF488 monomers were mixed with unlabeled NPM1 monomers at 1:9 ratio in 6 M guanidine HCl and refolded in dialysis against 10 mM Tris, 150 mM NaCl, 2 mM DTT, pH 7.5.

Recombinant p14<sup>ARF</sup> proteins were prepared as described<sup>26</sup>. Briefly, p14<sup>ARF</sup> and p14<sup>ARF</sup>  $\Delta$ H1-3 were expressed in *E. coli* BL21 cells grown at 37 °C in 30  $\mu$ g/ml Kanamycin supplemented LB medium. For

isotopic labeling to generate [<sup>13</sup>C,<sup>15</sup>N]-p14<sup>ARF</sup>, cells were grown in MOPS-based minimal media containing [<sup>13</sup>C<sub>6</sub>]-D-glucose and <sup>15</sup>NH<sub>4</sub>Cl (Cambridge Isotope Laboratories)<sup>53</sup>. For [<sup>13</sup>C]-p14<sup>ARF</sup> and [<sup>15</sup>N]-p14<sup>ARF</sup> labeled p14<sup>ARF</sup>, [<sup>13</sup>C<sub>6</sub>]-D-glucose/NH<sub>4</sub>Cl and D-glucose/<sup>15</sup>NH<sub>4</sub>Cl were used, respectively. At OD<sub>600nm</sub> = 0.8, 0.5 mM IPTG was added, cells were incubated at 37 °C for an additional 3 h and harvested by centrifugation at 3800  $\times$  g at 4 °C. Cells were resuspended in 50 mM Tris pH 8.0, 500 mM NaCl, 5 mM  $\beta$ -mercaptoethanol, and one SIGMAFAST protease inhibitor cocktail tablet (Sigma) and disrupted by sonication. The lysate was cleared by centrifugation at 30,000  $\times$  g at 4 °C and Urea was added to a final concentration of 6 M; this fraction was set aside. In parallel, the cell pellet was resuspended in 6 M Guanidine HCl, 0.1% Triton X-100, 5 mM  $\beta$ -mercaptoethanol and subjected to mechanical disruption followed by sonication. This fraction was cleared by centrifugation at 30,000  $\times$  g at 4 °C and the supernatant was removed, combined with the initial lysate, and purified by Ni-NTA-affinity chromatography on an ÄKTA FPLC (GE) using a linear gradient of 50 mM Tris pH 8.0, 500 mM NaCl, 5 mM  $\beta$ -mercaptoethanol and 500 mM Imidazole and further purified using C<sub>4</sub> HPLC (Higgins Analytical, Mountain View, CA, USA) with a H<sub>2</sub>O/CH<sub>3</sub>CN/0.1% trifluoroacetic acid solvent system.

To generate calibration curves for mEGFP and mRFP670 fluorescence, recombinant poly-histidine-tagged mRFP670 and mEGFP in pET28a (+) (Novagen) were expressed in BL21 (DE3) *Escherichia coli* cells (Millipore Sigma, Burlington, MA, USA). Cells were grown at 37 °C in LB medium supplemented with 30  $\mu$ g/ml of Kanamycin. At OD<sub>600nm</sub> = 0.8, 0.5 mM Isopropyl  $\beta$ -D-1 thiogalactopyranoside (IPTG) was added, cells were incubated at 37 °C for 3 h and harvested by centrifugation at 3800  $\times$  g at 4 °C. Proteins were purified from the soluble lysates fraction using Ni-NTA affinity chromatography. Affinity tags were removed via proteolytic cleavage with tobacco etch virus (TEV) protease and purified using a S75 10/300 (GE) gel filtration column on an ÄKTA FPLC (GE). Biliverdin HCl (Sigma-Aldrich) was dissolved into PBS, added to mRFP670 at a 2.5-fold molar excess and incubated at 37 °C for 3 hrs. Excess biliverdin was removed by buffer exchange using a centrifugal filtration device.

## Condensate formation for imaging

To prepare p14<sup>ARF</sup>-NPM1 and p14<sup>ARF</sup>  $\Delta$ H1-3-NPM1 condensates for fluorescence microscopy analysis, the recombinant p14<sup>ARF</sup> proteins (p14<sup>ARF</sup> and p14<sup>ARF</sup>  $\Delta$ H1-3) were resuspended from lyophilized powders using 100% dimethyl sulfoxide (DMSO) and added directly to solutions of NPM1, at room temperature, such that the final NPM1 concentrations were 10  $\mu$ M. The final buffer contained 10 mM Tris pH 7.5, 150 mM NaCl, 2 mM DTT, 1.67% DMSO. Condensate suspensions were incubated for 1 hr at room temperature before being transferred to 16-well CultureWell chambered slides (Grace BioLabs, Bend, OR, USA) pre-coated with PlusOne Repel Silane ES (GE Healthcare, Pittsburgh, PA, USA) and Pluronic F-127 (Sigma-Aldrich, St. Louis, MO, USA). Images were acquired on a 3i Marianas spinning disk confocal microscope (Intelligent Imaging Innovations Inc., Denver, CO, USA) using a 100 $\times$  oil immersion objective (N.A. 1.4).

## Small-angle neutron scattering

SANS experiments were performed on the extended q-range small-angle neutron scattering (EQ-SANS) beam line at the Spallation Neutron Source (SNS) at the Oak Ridge National Laboratory (ORNL). The detector was set at 4 m from the sample position. The choppers ran at 30 Hz in frame-skipping mode to give two wavelength bands: 2.5 Å to 6.1 Å and 9.4 Å to 13.1 Å. This configuration provided a q-range from -0.004 Å<sup>-1</sup> < q < 0.45 Å<sup>-1</sup>. The source aperture was 25 mm diameter and the sample aperture was 10 mm diameter.

To prepare p14<sup>ARF</sup>-NPM1 condensates for CV-SANS analysis recombinant p14<sup>ARF</sup> & p14<sup>ARF</sup>  $\Delta$ H1-3 proteins were resuspended from lyophilized powders in 100% deuterated dimethyl sulfoxide (DMSO)



and added directly to solutions of NPM1 at room temperature ( $-23\text{ }^{\circ}\text{C}$ ) to induce formation of phase-separated condensates. All samples contained 10 mM sodium phosphate pH 7, 150 mM NaCl, 2 mM TCEP. For condensate formation, p14<sup>ARF</sup> proteins and NPM1 were 40  $\mu\text{M}$ . Measurement of isolated [<sup>2</sup>H]-NPM1 was performed on a 50  $\mu\text{M}$  solution. Full scatter measurements were performed in buffer containing 100% D<sub>2</sub>O and using protonated proteins. For contrast variation measurements, the H<sub>2</sub>O/D<sub>2</sub>O ratios were adjusted to 84.9% D<sub>2</sub>O to match [<sup>2</sup>H]-NPM1, 44.7% for p14<sup>ARF</sup>, and 49.6% for p14<sup>ARF</sup>ΔHI-3. The match point for NPM1 was determined experimentally<sup>19</sup>. Due to the instability of p14<sup>ARF</sup> in solution, the match points for p14<sup>ARF</sup> and p14<sup>ARF</sup>ΔHI-3 were calculated using the MULCh contrast calculator tool<sup>55</sup>. The samples were loaded into 2 mm pathlength circular-shaped quartz cuvettes (Hellma USA, Plainville, NY) and SANS measurements were performed at 25  $^{\circ}\text{C}$  while the samples rotated on a tumbler to prevent droplets from settling out of suspension. Data reduction was performed using MantidPlot<sup>56</sup>. The measured scattering intensities were corrected for the detector sensitivity, the scattering contribution from the buffer and empty cells and re-scaled to an absolute scale using a calibrated standard<sup>57</sup>.

For p14<sup>ARF</sup>-NPM1 condensates under full scattering conditions, the scattering curve was fit to a broad peak model<sup>17</sup>(Eq 1):

$$I(q) = \frac{C_0}{1 + (\xi_0|q - q_0|)^{m_0}} + \frac{C_1}{1 + (\xi_1|q - q_1|)^{m_1}} + B \quad (1)$$

where,  $\xi_0$  is the correlation length from the scattering at high- $q$  and  $\xi_1$  is the correlation length from scattering at low- $q$ . The peak corresponds to the d-spacing ( $d_0 = \frac{2\pi}{q_0}$ ), *i.e.*, the characteristic distance between scattering inhomogeneities. The scaling exponent,  $\nu_0 = \frac{1}{m_0}$ , and  $B$  accounts for the background scattering. For [<sup>2</sup>H]-NPM1 in solution, the low- $q$  region was fit to the Guinier approximation (Eq. 2):

$$I(q) \approx I_0 e^{-\frac{q^2 R_g^2}{3}} \quad (2)$$

where,  $R_g$  is the radius of gyration. For NPM1-matched, p14<sup>ARF</sup>-detected conditions, scattering was fit to a broad peak model with a correlation length term<sup>58</sup>(Eq. 3):

$$I(q) = \frac{C_0}{1 + (\xi_0|q - q_0|)^{m_0}} + \frac{C_1}{1 + (\xi_1|q|)^{m_1}} + B \quad (3)$$

For p14<sup>ARF</sup>-matched, NPM1-detected conditions, scattering was fit to a correlation length model (Eq. 4):

$$I(q) = \frac{C_0}{1 + (\xi_0 q)^{m_0}} + B \quad (4)$$

For p14<sup>ARF</sup>ΔHI-3-NPM1 condensates, all scattering curves were fit to Eq. 3.

### Condensate formation for NMR analysis

To prepare p14<sup>ARF</sup>-NPM1 condensates for NMR analysis, recombinant unlabeled and isotopically enriched p14<sup>ARF</sup> proteins (including [U<sup>13</sup>C, <sup>15</sup>N]-p14<sup>ARF</sup>, [<sup>13</sup>C]-p14<sup>ARF</sup> and [<sup>15</sup>N]-p14<sup>ARF</sup>) were resuspended from lyophilized powders in 100% deuterated dimethyl sulfoxide (DMSO-d<sub>6</sub>) and added directly to solutions of NPM1 to induce formation of phase-separated p14<sup>ARF</sup>-NPM1 condensates. These condensates were formed at room temperature ( $-23\text{ }^{\circ}\text{C}$ ), such that the final p14<sup>ARF</sup> and NPM1 concentrations were 20  $\mu\text{M}$ . For assignment of p14<sup>ARF</sup> by solution-state NMR, a condensed phase was prepared by mixing 50  $\mu\text{M}$  [<sup>13</sup>C, <sup>15</sup>N]-p14<sup>ARF</sup> and 50  $\mu\text{M}$  NPM1-IDR. The final buffer contained 10 mM sodium phosphate pH 7.0, 150 mM NaCl, 2 mM TCEP, 0.015% NaN<sub>3</sub>, 1.67% DMSO-d<sub>6</sub>, 7% D<sub>2</sub>O. Low concentrations of DMSO-d<sub>6</sub> have no effect on the structure of NPM1 as confirmed previously by solution-

state NMR<sup>26</sup>. Following phase separation, samples were incubated for 20 min at room temperature. Samples were then ultracentrifuged at 436,000  $\times g$  for 2 h at 4  $^{\circ}\text{C}$  to pellet the condensates. The light phases were removed prior to NMR analysis.

### Solution-state NMR spectroscopy

Solution-state NMR experiments were performed on Bruker AVANCE NEO spectrometers. Measurements of p14<sup>ARF</sup> were made on spectrometers operating at 14.1 T and 18.8 T (<sup>1</sup>H Larmor frequencies of 600 MHz and 800 MHz, respectively) using 5 mm triple-resonance 1H/13C/15N TCI and <sup>13</sup>C-optimized TXO cryo-probes. Measurements of NPM1 were made on a spectrometer operating at 18.8 T, equipped with a TXO cryoprobe optimized for <sup>13</sup>C. Spectra were processed in Topspin 4.0 or NMRPipe and analyzed in Sparky within the NMRBox virtual environment<sup>59</sup>.

The concentration of p14<sup>ARF</sup> within the p14<sup>ARF</sup>-NPM1 condensed phase is  $\sim 200\text{ }\mu\text{M}$ <sup>26</sup>, which lies close to the limit of detection for most triple resonance experiments needed to make backbone assignments<sup>60</sup>. Therefore, we utilized a condensate containing p14<sup>ARF</sup> and the NPM1 IDR (amino acids 119–240), which we found contains  $\sim 1\text{ mM}$  p14<sup>ARF</sup> (Supplementary Fig. 3A-F). For backbone resonance assignment of [<sup>13</sup>C, <sup>15</sup>N]-p14<sup>ARF</sup> within the condensed phase with NPM1 IDR, 2D and 3D spectra<sup>60–73</sup>, were collected at room temperature (298 K) and optimized for signal to noise and acquisition times. <sup>1</sup>H and <sup>15</sup>N chemical shift assignments were then transferred onto 2D-TROSY-HSQC spectra (transverse relaxation optimized spectroscopy) collected for the [<sup>13</sup>C, <sup>15</sup>N]-p14<sup>ARF</sup>-NPM1 condensate (Supplementary Fig. 3G). Both spectra were nearly identical (Supplementary Fig. 3H).

In solution measurements of NPM1 structure and dynamics were performed on 65  $\mu\text{M}$  [<sup>2</sup>H, <sup>15</sup>N]-NPM1 in 10 mM sodium phosphate pH=7.0, 150 mM NaCl, 2 mM DTT, 10% D<sub>2</sub>O at 25 $^{\circ}\text{C}$  at room temperature (298 K) at 800 MHz. Chemical shift assignments for NPM1 were transferred from published values<sup>19,26</sup>. 2D <sup>1</sup>H-<sup>15</sup>N TROSY-HSQC<sup>61</sup>,  $R_1$ <sup>74,75</sup>,  $R_2$ <sup>74,75</sup> and <sup>15</sup>N-CPMG<sup>76,77</sup> experiments were optimized for signal to noise and acquisition times. <sup>1</sup>H-<sup>15</sup>N NOE values were calculated as the ratio between peak intensities in spectra recorded with and without <sup>1</sup>H saturation. The <sup>15</sup>N relaxation rates,  $R_1$  and  $R_2$ , were determined by fitting cross-peak intensities, measured as a function of variable delay periods, to a single-exponential decay. <sup>15</sup>N-CPMG relaxation dispersion was fitted using the protein dynamics toolset in the Bruker Dynamics Center 2.5.6 with the following fitted function alternatives:

$$f(x) = c \quad (5)$$

$$f(x) = R_{20} + \frac{\Phi}{K_{\text{ex}}} \left[ 1 - \frac{x}{K_{\text{ex}}} \tanh\left(\frac{K_{\text{ex}}}{x}\right) \right] \quad (6)$$

$$f(x) = R_{20} + K_{\text{ex}} \left[ 1 - \frac{\sin(\Delta\omega x)}{\Delta\omega x} \right] \quad (7)$$

where  $R_{20}$  is the effective relaxation rate,  $K_{\text{ex}}$  is the exchange rate,  $\Delta\omega$  is the chemical shift difference between states A and B, and  $\Phi = P_A P_B \Delta\omega^2$ . Systematic errors were estimated based on peak intensities. All repetition experiments were assessed to calculate the largest difference in peak intensities per peak, which was used as a systematic error per peak for each mixing time. Fit parameter error estimation was performed using Monte-Carlo simulation. Fitted parameters were calculated with a 95% confidence interval.

### Solid-state NMR spectroscopy

Solid-state NMR experiments were performed on a Bruker Avance NEO spectrometer operating at 14.1 T (<sup>1</sup>H Larmor frequency of 600 MHz) using a Bruker MAS CryoProbe<sup>TM</sup>, a cryogenically cooled magic-angle spinning (MAS) triple resonance (HCN) probe head<sup>78</sup>. The samples

were packed in specially designed 3.2 mm MAS rotors with Teflon inserts to ensure proper centering of the p14<sup>ARF</sup>-NPM1 condensate samples. Detailed description of the acquisition parameters can be found in Supplementary Table 4. In general, all the MAS experiments were performed at MAS speeds between 10–15 kHz. Typical radio-frequency (RF) fields used in the experiments for the <sup>1</sup>H, <sup>13</sup>C and <sup>15</sup>N channels were 80–100 kHz, 60–65 kHz and 40 kHz, respectively. Double cross polarization (CP), dipolar assisted rotational resonance (DARR) and COmbined R2vn-Driven (CORD) mixing requires lower RF fields and are reported in Supplementary Table 4. Contact times for CP and double CP were typically 1 ms with recycle delays of 2 s. The CP-MAS NMR acquisition times varying from 1–2 h for two-dimensional (2D) NCO<sup>79,80</sup> and NCaCX experiments<sup>81–83</sup> 2D experiments) to several hours (7–10 h) for the 2D CC correlation experiments (with DARR, CORD or insensitive nuclei enhanced by polarization transfer (INEPT) mixing). Three-dimensional (3D) experiments were recorded over 1.5 (3D NCOX<sup>79,80</sup>) and 2.5 days (3D NCaCx, through co-addition of two experiments of one day each and another of 10 h; 34 h of acquisition in total). The NHHc experiment used to probe contacts between the <sup>15</sup>N-p14<sup>ARF</sup> and the <sup>13</sup>C-p14<sup>ARF</sup> molecules within condensates with NPM1, based on proton spin diffusion between <sup>15</sup>N-coupled amide protons (in one p14<sup>ARF</sup> molecule and <sup>13</sup>C-coupled aliphatic protons in another p14<sup>ARF</sup> molecule), required the longest experimental time: two spectra acquired with identical parameters were co-added; these were acquired for 3 days and 9 h, respectively. All spectra were referenced using adamantane (<sup>13</sup>C δ = 38.5 ppm).

### Cellular imaging

Fluorescence microscopy imaging for analysis of live DLD-1<sup>NPM1-G</sup> cell nucleoli was performed on a Zeiss LSM 980 Airyscan 2 inverted microscope, with a 40x Plan Apochromat (N.A. 1.1) objective (mEGFP *I*<sub>ex</sub> = 492 nm, miRFP670 *I*<sub>ex</sub> = 653 nm; *I*<sub>em</sub> = 300–720 nm). High-throughput fluorescence imaging of virally transduced DLD-1<sup>NPM1-G</sup> clones and FRAP experiments were performed using a 3i Marianas spinning disk confocal microscopes (Intelligent Imaging Innovations Inc., Denver, CO, USA) with a 40x air objective and 100x oil immersion objective (N.A. 1.4), respectively. Cells were maintained at 37 °C, 5% CO<sub>2</sub> within an enclosed incubator during live cell imaging experiments.

### Endogenously-tagged cell line generation

Endogenously C-terminally mEGFP-tagged NPM1 in DLD-1 cells (DLD-1<sup>NPM1-G</sup>) were generated using CRISPR-Cas9 technology in the Center for Advanced Genome Engineering (St. Jude Children's Research Hospital). The donor homology directed repair (HDR) template containing a (GGG)<sub>5</sub> linker DNA coding sequence upstream of the mEGFP sequence flanked by ~800 bases homology arms was synthesized and blunt-end cloned into pUCS7 (the plasmid pUCS7\_NPM1-mEGFP\_HDR donor repair template, CAGE117.g1.meGFP donor) by Bio Basic. Briefly, 500,000 DLD1 cells were transiently co-transfected with pre-complexed ribonuclear proteins (RNPs) consisting of 100 pmol of chemically modified sgRNA (CAGE117.NPM1.g1, 5'-UCCAGGCUAU-CAAGAUCUC-3', Synthego), 33 pmol of Cas9 protein (St. Jude Protein Production Core), 500 ng of plasmid donor. The transfection was performed via nucleofection (Lonza, 4D-Nucleofector™ X-unit) using solution P3 and program CA-137 in a small (20 μl) cuvette according to the manufacturer's recommended protocol. Single cells were sorted based on viability five days post-nucleofection into 96-well plates containing prewarmed media and clonally expanded. Clones were screened and verified for the desired modification using PCR-based assays and confirmed via sequencing. Final clones were authenticated using the PowerPlex Fusion System (Promega) performed at the Hartwell Center (St. Jude).

The sequence of the HDR donor template for NPM1-mEGFP knock-in is (5'-3'; lowercase: homology arms; uppercase: mEGFP; bold uppercase: (GGG)<sub>5</sub> linker; italics uppercase: silent blocking mutations):

```
ctcaggtgatccaacaccttggcctcttaaagtgctgggattacagggatgagccaccat
gcctggccagctgtttttttgttggttgtttttgttttggatccatctgtagtgatcttggctc
actgcaacctctgctcttgggctcaggcagctctccacctcagcctctgagtagctgggcc
tctgttagttgcaccaccaagcctggtaattttgcattttagtagacagggttccacatg
ttgccaggctggctcaaatctgagctgaagtgtctgcccctcagctcccaaatgtagc
tagggattacaggcgtgagccaccatgcttagcctcagcatatgttttctaaatgtacacat
gcccaggcacacatgcacaggcaattcagaataagtttctgggtttatgtaactttattggc
aaatctggccaactctaaagctgatctcgggagatgaagtggaaagtaacattggccat
gggtctctgttcttctgttgattccttaagtaataatgtaactataaataattattagtata
ttgtcacattttatgactgattaagtgtttggaattaatactatcagtagataaatttctgg
agtcacatctttatcagtagtaactctggtgtagaataaaaaatagatgtgtaactatgc
aaagagacatttaatttattgatgtctatgaagtgttgggttcttaaccacattttttttt
ttccaggctattcaagaCctGtggaAtggCgAaaAAGCctGGGAGGAAGCGGAG
GTTCTGGCGGTAGTGGTGGATCTGGCGGCAGCATGGTTTCCAAGGG
CGAAGAAGTGTTCACCGCGTGGTGCCCATCTGTGGTGAAGCTGAGC
GGGATGTGAACCGCCACAAGTTAGCGTTAGCGGCGGAAGGCGAAGG
GGATGCCACATACGGAAAGCTGACCCTGAAGTTCATCTGCACCACC
GGCAAGCTGCCTGTGCCTTGGCCTACACTGGTACCACACTGACATA
CGGCGTGCAGTGCTTACGAGATACCCCGACCATATGAGCAGCAGC
ACTTCTCAAGAGCGCCATGCCTGAGGGCTACGTGCAAGAGCGGACC
ATCTTCTTAAGGACGACGGCAACTACAAGACCAGGGCCGAAGTGAA
GTTGAGGGCGACACCCTGGTCAACCGGATCGAGCTGAAGGGCAT
CGACTTCAAAGAGGACGGCAACATCTGGGCCACAAGCTCGAGTAC
AACTACAACAGCCACAACGTGTACATCTGGCCGACAAGCAGAAAAA
CGGCATCAAAGTGAACCTCAAGATCCGGCACAACATCGAGGACGG
CTCTGTGCAGCTGGCCGATCACTACCAGCAGAACACACCCTCGGAG
ATGGCCCTGTGCTGCTGCCGATAACCCTACCTGAGCACCAGAGC
AAGCTGAGCAAGGACCCCAACGAGAAGCGGGACCACATGGTGCTGCT
GGAATTTGTGACAGCCCGGAATCACCTCGGCATGGATGAGCTGT
ACAAGTAAgaaaatagtttaacaatttggtaaaaaatttccgtcttattctgttaaca
gttgatctgctgtcctttataatgagagtgagaacttccctaccgttttgataaat
gtgtccaggttctattgccaagaatgtgtgtccaaaatgctgtttatgatttaaatggaa
ctccacccttctggttttaagtatgtatggaatgtatgagacatagtagtagcgggtg
tcagacatggaaatggggggagacaaaatatacatgtgaaataaaacagatttaataaa
tagcacgggttctattgacttatttaactgctttataacttggtaaaataatgtagtta
ggaatggcaaatagtctgttaaaattctatgagaatgctcctgcccctccctcaatattctctg
gagtaaccattttcatcataaggatttagtctgtgttccaccctctgatgatgtaacaatt
attataactatgcaacatgtttccaaatgttccattagacctctatctgctattctagcctcact
gcaagaaaatgtggcatgttaaaacagcttaaaagcagctttcaacctgtatggttttcccc
aggctggagtgcagtgccacaatctcagcttattgagcttctgcttctgggttaagcaggt
ctctgctcagctcccaagtagctgggattacaggtgtgagccaccagccggtaatttt
gtatttttagtagaga
```

The three pairs of primers used for PCR were as follows: 5' junction primers, including CAGE117.gen.F2 (forward, 5'-TGACCTGA-GAACCATTGGC-3') and CAGE117.junc.meGFP.DS.R2 (reverse, 5'-GTTACATCCCCGTCCAGTT-3'); 3' junction primers, including CAGE117.junc.meGFP.DS.F2 (forward, 5'-GCTGCCGATAACCACTACC-3') and CAGE117.gen.R2 (reverse, 5'-AGGCAGAACATATAAAGGTGC TAAT-3'); and zygosity confirmation primers, including CAGE117.DS.F (forward, 5'-AGTAACTCTCTGGTGGTAGAATGA-3') and CAGE117.DS.R (reverse, 5'-CCAAGCAAAGGTGGAGTTC-3').

### Lentiviral transduction and generation of cell lines

Lentiviral vectors were used to make lentiviral particles by the Vector Development and Production Shared Resource at St. Jude Children's Research Hospital. Cells were transduced with virus in the presence of 10 μg/ml polybrene (Sigma). For pINDUCER20 lentivirus transduced cells, the selection by G418 (500 μg/ml) lasted until mock-transfected, control cells were completely eliminated, and the cells were constantly maintained in the culture medium containing G418 at 250 μg/ml.

### Single-cell cloning

Each population of the virally transduced, G418 resistant cells were sorted one cell/well into three 96-well plates. After growing in G418-containing media for 710 days, each viable single colony was further

passed into two corresponding wells in one Nunc 96-well cell culture treated plate (ThermoFisher) and one glass bottom black 96-well plate (Greiner Bio-One, Cat. #655891). The clones in the glass bottom 96-well plates were treated with 1  $\mu\text{g}/\text{ml}$  doxycycline to induce the expression of miRFP670-tagged protein in cells, and the expression levels were quantified by measuring miRFP670 fluorescence intensity in the live cells using fluorescence microscopy. Single cell clones in the corresponding wells in the Nunc 96-well plates, which could express miRFP670-tagged protein at high, medium, or low levels, were selected and expanded. As miRFP670 requires the cofactor biliverdin for fluorescence<sup>84</sup>, the protein expression levels in these single-cell clones were further assessed by immunoblotting analysis.

### Immunoblotting

Gel electrophoresis was performed using 25–40  $\mu\text{g}$  protein extracted from TRIZOL cell lysates or equal volumes of protein extracts from sucrose gradient fractions in NuPAGE mini protein gels (Invitrogen), transferred for 1.5 h at 30 volt to PVDF Transfer Membrane with low background fluorescence (Millipore). After Ponceau S staining, the membranes were blocked for 1 h in 5% non-fat milk in 1 $\times$  PBS, then incubated with primary antibodies diluted in 2.5% BSA in PBST solution (1 $\times$  PBS, 0.2% Tween-20) overnight at 4  $^{\circ}\text{C}$  with gentle agitation. Membranes were rinsed 4 $\times$  in PBST buffer before incubating in fluorescence conjugated secondary antibodies diluted in 1% non-fat milk in 1 $\times$  PBS with 0.02% SDS for 45 min at room temperature in the dark. After washing with 4 $\times$  in PBST, the blots were scanned with the ChemiDoc Imaging System (Bio-Rad). The primary antibodies were used as follows: rabbit monoclonal anti-Cyclophilin B (Cell Signaling, 43603) at 1:1500–1:2000 dilution; rabbit monoclonal anti-GAPDH (Cell Signaling, 5174) at 1:2500 dilution; mouse monoclonal anti-NPM1 (ThermoFisher Scientific, 32-5200) at 1:1000 dilution; mouse monoclonal anti-p14<sup>ARF</sup> (Cell Signaling, 2407) at 1:1000–1:15000 dilution; mouse monoclonal anti-GAPDH (Santa Cruz, sc-47724) at 1:2500 dilution; and rabbit polyclonal anti-p14<sup>ARF</sup> (Novus, NB200-111) at 1:2000 dilution.

### Cell treatments

Treatment of doxycycline inducible cells was performed with doxycycline at 1  $\mu\text{g}/\text{ml}$  or serially diluted from the stock solution of 1 mg/ml for the indicated times. Unless otherwise indicated, single clones of cells were treated with doxycycline at the concentrations as follows: 1000 ng/ml (p14<sup>ARF</sup>-iRFP clones), 50 ng/ml (p14<sup>ARF</sup>  $\Delta$ H1-3-iRFP clone H5), 20 ng/ml (iRFP clone H9), or 10 ng/ml (p14<sup>ARF</sup>  $\Delta$ H1-3-iRFP clone C10, iRFP clone A6). The time course samples were harvested at the same time.

### Cell growth assays

Aliquots of cell suspensions were seeded in 96- or 24-well plates at 5000 or 10,000 cells per well, respectively. After culturing for 20–24 h, the cells were counted for the starting time point and/or subjected to treatments as needed, and then cultured for the indicated times. For cell counting, existing culture medium in each well was replaced with fresh culture medium containing 10-fold diluted Cell Counting Kit-8 (CCK-8, APEX-BIO), and the absorbance at 450 nm was measured after 1–2 h of incubation. Cell growth was calculated as the ratio of  $A_{450}$  at later time points relative to that of the starting time point. The relative cell viability was expressed as the ratio of  $A_{450}$  of the treated versus that of untreated controls cells. Biological replicates were performed separately at different times.

### Fluorescence recovery after photobleaching

Analysis of fluorescence recovery after photo-bleaching (FRAP) images to determine the apparent diffusion coefficient ( $D_{\text{App}}$ ) and

percent mobility was performed following a modified version of the protocol from<sup>85</sup>, using in-house pipelines written in Python (Supplementary Fig. 8). For FRAP in live cells, all images were corrected ( $I(t)_{\text{corr}}$ ) to account for background fluorescence ( $I(t)_{\text{bkgd}}$ ) and for photofading and irreversible loss of molecules during the bleach event, using the mean intensity of the cell nucleus ( $I(t)_{\text{cell}}$ ) (Eq. 8), where:

$$I(t)_{\text{corr}} = \frac{I(t) - I(t)_{\text{bkgd}}}{I(t)_{\text{cell}} - I(t)_{\text{bkgd}}} \quad (8)$$

Here, the background and mean nuclear intensities were extracted from freehand drawn regions of interest (ROI) using the Slidebook 6.0 (Intelligent Imaging Innovations, Gottingen, Germany). For FRAP of droplets, all images were corrected using an unbleached reference droplet ( $I(t)_{\text{ref}}$ ) (Eq. 9).

$$I(t)_{\text{corr}} = \frac{I(t) - I(t)_{\text{bkgd}}}{I(t)_{\text{ref}} - I(t)_{\text{bkgd}}} \quad (9)$$

The FRAP ROI intensity ( $R(t)$ ) was then rescaled ( $R(t)_{\text{norm}}$ ), using the mean ROI intensity for all ten image frames preceding the bleach event ( $\langle R(t)_{\text{pre-bleach}} \rangle$ ) and the ROI intensity immediately following the bleach event ( $R_{\text{post-bleach}}$ ) (Eq. 10), where:

$$R(t)_{\text{norm}} = \frac{R(t) - R_{\text{post-bleach}}}{\langle R(t)_{\text{pre-bleach}} \rangle - R_{\text{post-bleach}}} \quad (10)$$

The half-time for recovery ( $t_{1/2}$ ) was then extracted from the recovery curve by fitting to the equation from<sup>86</sup> using the curve\_fit function in scipy (Eq. 11):

$$R(t) = \frac{[R_{\text{post-bleach}} + R_{\infty} \left( \frac{t}{t_{1/2}} \right)]}{1 + \left( \frac{t}{t_{1/2}} \right)} \quad (11)$$

where,  $R_{\infty}$  is the ROI intensity after full recovery. The percent mobility ( $M$ ) was calculated using Eq 12:

$$M = \frac{\langle R_{\infty}(t) \rangle}{\langle R(t)_{\text{pre-bleach}} \rangle} \quad (12)$$

where, ( $\langle R_{\infty}(t) \rangle$ ) is the mean ROI intensity of the last ten image frames of the signal plateau region.

Prior to extracting the diffusion coefficient ( $D_{\text{App}}$ ), image correction for diffusion during the bleach event ( $I_{\text{norm}}$ ) was performed<sup>85,87</sup>. The post-bleach image was first normalized using the image frames preceding ( $I_{\text{pre-bleach}}$ ) and immediately following the bleach event ( $I_{\text{post-bleach}}$ ) (Eq. 13).

$$I_{\text{norm}} = \frac{I_{\text{post-bleach}}}{I_{\text{pre-bleach}}} \quad (13)$$

The normalized post-bleach profile was then fit to an exponential of a Gaussian laser profile ( $\varphi$ ) using the curve\_fit function in scipy (Eq. 14):

$$\varphi(x, y) = F_i \exp \left[ -K \exp \left[ -\frac{2(x^2 + y^2)}{r_e^2} \right] \right] \quad (14)$$



where, ( $r_e$ ) is the effective bleach radius.  $D_{App}$  was then calculated using  $t_{1/2}$  and the nominal bleach radius ( $r_n$ ) (Eq. 15).

$$D_{App} = \frac{r_e^2 + r_n^2}{8t_{1/2}} \quad (15)$$

### Image analysis and quantification

Prior to analysis, images were converted into tiff format using Slidebook 6.0 (Intelligent Imaging Innovations, Gottingen, Germany) or Image J<sup>88</sup>. Image segmentation was performed using an in-house pipeline written in Python (Supplementary Fig. 10). Segmentation of nuclei and nucleoli were performed using the NPM1 signal; NPM1-GFP fluorescence was used for segmenting live DLD-1<sup>NPM1-G</sup> cell images. 3D image stacks were first converted to 2D images through maximum intensity projection. Prior to segmentation of nuclei, the Gaussian kernel with variable standard deviation ( $\sigma$ ) from scikit-image was first applied (for Airyscan DLD-1<sup>NPM1-G</sup> cell images  $\sigma = 4$ ).

Prior to segmentation of nucleoli, a Gaussian kernel with  $\sigma = 0.33$  was applied. Segmentation was performed using the multi-Otsu algorithm from scikit-image using 3 classes as input. Nuclear masks were found at the 0<sup>th</sup> threshold and nucleolar masks were found at the 1<sup>st</sup> threshold. Masked pixels were then clustered using the density-based spatial clustering of applications with noise (DBSCAN) algorithm as implemented in scikit-learn. Segmented cells along with their nuclear and nucleolar masks were visualized using the imshow function from matplotlib. All segmented cell masks were verified by manual observation and improperly segmented cells were removed prior to quantification.

To quantify the extent of recombinant p14<sup>ARF</sup>-NPM1 phase separation the index of dispersion (IOD) was calculated for  $\geq 4$  imaging areas of 512  $\times$  512 pixels (64  $\times$  64  $\mu\text{m}$ ), (Eq. 16):

$$IOD = \frac{\sigma^2}{\mu} \quad (16)$$

where,  $\sigma^2$  is the variance and  $\mu$  is the mean fluorescence intensity. To quantify the transfer free energy the following was used (Eq. 17):

$$\Delta G_{tr} = -RT \log\left(\frac{I_{DP}}{I_{LP}}\right) \quad (17)$$

where, R is the universal gas constant, T is the temperature,  $I_{DP}$  is the mean dense phase fluorescence intensity, and  $I_{LP}$  is the mean light phase fluorescence intensity.

### Statistics

The numbers of independent replicates for each experiment are provided in the figure legends. Unless stated in figure legends, all values represent means  $\pm$  SD.  $p < 0.05$  was considered statistically significant. Asterisks denote statistical significance as follows: n.s. = not significant; \* $p < 0.05$ ; \*\* $p < 0.01$ ; \*\*\* $p < 0.001$ ; and \*\*\*\* $p < 0.0001$ . For all box and whiskers plots, each box extends from the first to the third quartiles, with the line or center point representing the median, and the whiskers extending from the box to the furthest point within 1.5x the interquartile range. If shown, flier points represent outlier points beyond the whiskers.

### Reporting summary

Further information on research design is available in the Nature Portfolio Reporting Summary linked to this article.

### Data availability

The data that support the findings of this study are available without restriction from the corresponding author upon request. The NPM1

structures used for DSSP<sup>89</sup> secondary structure analysis are available from the Protein Data Bank, including PDB 4N8M (OD), and PDB 2LLH (NBD). NMR assignments derived from the analyzes of p14<sup>ARF</sup> and NPM1 are available from the Biological Magnetic Resonance Bank, including BMRB 52628 (solid-state NMR assignments for the [<sup>13</sup>C,<sup>15</sup>N]-p14<sup>ARF</sup>-NPM1 condensate), BMRB 52629 (solution-state NMR assignments for the [<sup>13</sup>C,<sup>15</sup>N]-p14<sup>ARF</sup>-NPM1 condensate), BMRB 52630 (solution-state NMR assignments for the [<sup>13</sup>C,<sup>15</sup>N]-NPM1-p14<sup>ARF</sup> condensate). Source data are provided with this paper.

### Code availability

Original code generated during this study are available on Figshare (FRAP processing pipeline; <https://doi.org/10.6084/m9.figshare.27221664>, and cell image segmentation pipeline <https://doi.org/10.6084/m9.figshare.27221679>).

### References

- Sherr, C. J. Divorcing ARF and p53: an unsettled case. *Nat Rev Cancer* **6**, 663–673 (2006).
- Bertwistle, D., Sugimoto, M. & Sherr, C. J. Physical and functional interactions of the Arf tumor suppressor protein with nucleophosmin/B23. *Mol Cell Biol* **24**, 985–996 (2004).
- Korgaonkar, C. et al. Nucleophosmin (B23) targets ARF to nucleoli and inhibits its function. *Mol Cell Biol* **25**, 1258–1271 (2005).
- Quin, J. E. et al. Targeting the nucleolus for cancer intervention. *Bba-Mol Basis Dis* **1842**, 802–816 (2014).
- Kuo, M. L., den Besten, W., Bertwistle, D., Roussel, M. F. & Sherr, C. J. N-terminal polyubiquitination and degradation of the Arf tumor suppressor. *Gene Dev* **18**, 1862–1874 (2004).
- Colombo, E. et al. Nucleophosmin is required for DNA integrity and p19(Arf) protein stability. *Mol Cell Biol* **25**, 8874–8886 (2005).
- Gonzalez-Arzola, K. et al. Nucleus-translocated mitochondrial cytochrome c liberates nucleophosmin-sequestered ARF tumor suppressor by changing nucleolar liquid-liquid phase separation. *Nat Struct Mol Biol* **29**, 1024–102 (2022).
- Lee, S., Cho, Y. E., Kim, S. H., Kim, Y. J. & Park, J. H. GLTSCR2 promotes the nucleoplasmic translocation and subsequent degradation of nucleolar ARF. *Oncotarget* **8**, 16293–16302 (2017).
- Llanos, S., Clark, P. A., Rowe, J. & Peters, G. Stabilization of p53 by p14(ARF) without relocation of MDM2 to the nucleolus. *Nat Cell Biol* **3**, 445–452 (2001).
- Lee, C., Smith, B. A., Bandyopadhyay, K. & Gjerset, R. A. DNA damage disrupts the p14ARF-B23(nucleophosmin) interaction and triggers a transient subnuclear redistribution of p14ARF. *Cancer Res* **65**, 9834–9842 (2005).
- David-Pfeuty, T. & Nouvian-Dooghe, Y. Human p14(Arf): an exquisite sensor of morphological changes and of short-lived perturbations in cell cycle and in nucleolar function. *Oncogene* **21**, 6779–6790 (2002).
- Rubbi, C. P. & Milner, J. Disruption of the nucleolus mediates stabilization of p53 in response to DNA damage and other stresses. *EMBO J* **22**, 6068–6077 (2003).
- Tago, K., Chiocca, S. & Sherr, C. J. Sumoylation induced by the Arf tumor suppressor: A p53-independent function. *P Natl Acad Sci USA* **102**, 7689–7694 (2005).
- Bothner, B. et al. Defining the molecular basis of Arf and Hdm2 interactions. *J Mol Biol* **314**, 263–277 (2001).
- Brangwynne, C. P., Mitchison, T. J. & Hyman, A. A. Active liquid-like behavior of nucleoli determines their size and shape in *Xenopus laevis* oocytes. *Proc Natl Acad Sci USA* **108**, 4334–4339 (2011).
- Feric, M. et al. Coexisting liquid phases underlie nucleolar sub-compartments. *Cell* **165**, 1686–1697 (2016).
- Mitrea, D. M. et al. Nucleophosmin integrates within the nucleolus via multi-modal interactions with proteins displaying R-rich linear motifs and rRNA. *Elife* **5** <https://doi.org/10.7554/eLife.13571> (2016).

18. Mitrea, D. M. et al. Self-interaction of NPM1 modulates multiple mechanisms of liquid-liquid phase separation. *Nat Commun* **9**, 842 (2018).
19. White, M. R. et al. C9orf72 Poly(PR) dipeptide repeats disturb biomolecular phase separation and disrupt nucleolar function. *Mol Cell* **74**, 713–728 e716 (2019).
20. Rizos, H., Darmanian, A. P., Holland, E. A., Mann, G. J. & Kefford, R. F. Mutations in the INK4a/ARF melanoma susceptibility locus functionally impair p14ARF. *J Biol Chem* **276**, 41424–41434 (2001).
21. Zhang, Y. & Xiong, Y. Mutations in human ARF exon 2 disrupt its nucleolar localization and impair its ability to block nuclear export of MDM2 and p53. *Mol Cell* **3**, 579–591 (1999).
22. Pappu, R. V., Wang, X., Vitalis, A. & Crick, S. L. A polymer physics perspective on driving forces and mechanisms for protein aggregation. *Arch Biochem Biophys* **469**, 132–141 (2008).
23. Farag, M. et al. Condensates formed by prion-like low-complexity domains have small-world network structures and interfaces defined by expanded conformations. *Nat Commun* **13**, 7722 (2022).
24. Ader, C. et al. Amyloid-like interactions within nucleoporin FG hydrogels. *P Natl Acad Sci USA* **107**, 6281–6285 (2010).
25. Conicella, A. E., Zerze, G. H., Mittal, J. & Fawzi, N. L. ALS mutations disrupt phase separation mediated by  $\alpha$ -helical structure in the TDP-43 low-complexity c-terminal domain. *Structure* **24**, 1537–1549 (2016).
26. Gibbs, E., Perrone, B., Hassan, A., Kummerle, R. & Kriwacki, R. NPM1 exhibits structural and dynamic heterogeneity upon phase separation with the p14ARF tumor suppressor. *J Magn Reson* **310** <https://doi.org/10.1016/j.jmr.2019.106646> (2020).
27. Ferrolino, M. C., Mitrea, D. M., Michael, J. R. & Kriwacki, R. W. Compositional adaptability in NPM1-SURF6 scaffolding networks enabled by dynamic switching of phase separation mechanisms. *Nature Communications* **9** (2018). 10.1038/s41467-018-07530-1
28. Holehouse, A. S., Das, R. K., Ahad, J. N., Richardson, M. O. G. & Pappu, R. V. CIDER: resources to analyze sequence-ensemble relationships of intrinsically disordered proteins. *Biophys J* **112**, 16–21 (2017).
29. Somjee, R., Mitrea, D. M. & Kriwacki, R. W. Exploring Relationships between the Density of Charged Tracts within Disordered Regions and Phase Separation. *Pacific Symposium on Biocomputing 2020*, 207–218 (2020).
30. Buchan, D. W. A. & Jones, D. T. The PSIPRED protein analysis workbench: 20 years on. *Nucleic Acids Res.* **47**, W402–W407 (2019).
31. Goldschmidt, L., Teng, P. K., Riek, R. & Eisenberg, D. Identifying the amyloids, proteins capable of forming amyloid-like fibrils. *Proc Natl Acad Sci USA* **107**, 3487–3492 (2010).
32. Shibayama, M. Small-angle neutron scattering on polymer gels: phase behavior, inhomogeneities and deformation mechanisms. *Polym J.* **43**, 18–34 (2011).
33. Riback, J. A. et al. Innovative scattering analysis shows that hydrophobic disordered proteins are expanded in water. *Science* **358**, 238–241 (2017).
34. Frieberg, B. R. et al. Viscoplastic fracture transition of a biopolymer gel. *Soft Matter* **14**, 4696–4701 (2018).
35. Lange, A., Luca, S. & Baldus, M. Structural constraints from proton-mediated rare-spin correlation spectroscopy in rotating solids. *J Am Chem Soc* **124**, 9704–9705 (2002).
36. Etzkorn, M., Bockmann, A., Lange, A. & Baldus, M. Probing molecular interfaces using 2D magic-angle-spinning NMR on protein mixtures with different uniform labeling. *J Am Chem Soc* **126**, 14746–14751 (2004).
37. Riback, J. A. et al. Composition-dependent thermodynamics of intracellular phase separation. *Nature* **581**, 209–220 (2020).
38. Luchinat, E. et al. Identification of a novel nucleophosmin-interaction motif in the tumor suppressor p14arf. *Febs J* **285**, 832–847 (2018).
39. Frottin, F. et al. The nucleolus functions as a phase-separated protein quality control compartment. *Science* **365**, 342–344 (2019).
40. Kato, S. et al. Understanding the function-structure and function-mutation relationships of p53 tumor suppressor protein by high-resolution missense mutation analysis. *P Natl Acad Sci USA* **100**, 8424–8429 (2003).
41. Rodrigues, N. R. et al. p53 mutations in colorectal cancer. *Proc Natl Acad Sci USA* **87**, 7555–7559 (1990).
42. Esteller, M. et al. Hypermethylation-associated inactivation of p14(ARF) is independent of p16(INK4a) methylation and p53 mutational status. *Cancer Research* **60**, 129–133 (2000).
43. Hsu, P. D., Lander, E. S. & Zhang, F. Development and applications of CRISPR-Cas9 for genome engineering. *Cell* **157**, 1262–1278 (2014).
44. Shcherbakova, D. M. et al. Bright monomeric near-infrared fluorescent proteins as tags and biosensors for multiscale imaging. *Nature Communications* **7** <https://doi.org/10.1038/ncomms12405> (2016).
45. Sugimoto, M., Kuo, M. L., Roussel, M. F. & Sherr, C. J. Nucleolar Arf tumor suppressor inhibits ribosomal RNA processing. *Molecular Cell* **11**, 415–424 (2003).
46. Jacobs, W. M. & Frenkel, D. Phase transitions in biological systems with many components. *Biophys J* **112**, 683–691 (2017).
47. Siemer, A. B. Advances in studying protein disorder with solid-state NMR. *Solid State Nucl Mag* **106** <https://doi.org/10.1016/j.ssnmr.2020.101643> (2020).
48. Brady, S. N., Yu, Y., Maggi, L. B. & Weber, J. D. ARF impedes NPM/B23 shuttling in an Mdm2-sensitive tumor suppressor pathway. *Mol Cell Biol* **24**, 9327–9338 (2004).
49. Rizos, H. et al. Physical and functional interaction of the p14ARF tumor suppressor with ribosomes. *Journal of Biological Chemistry* **281**, 38080–38088 (2006).
50. Bothner, B., Aubin, Y. & Kriwacki, R. W. Peptides Derived From Two Dynamically Disordered Proteins Self-assemble Into Amyloid-like Fibrils. *J Am Chem Soc* **125**, 3200–3201 (2003).
51. Sivakolundu, S. G. et al. Intrinsically unstructured domains of Arf and Hdm2 form bimolecular oligomeric structures in vitro and in vivo. *J Mol Biol* **384**, 240–254 (2008).
52. DiGiammarino, E. L., Filippov, I., Weber, J. D., Bothner, B. & Kriwacki, R. W. Solution structure of the p53 regulatory domain of the p19Arf tumor suppressor protein. *Biochemistry* **40**, 2379–2386 (2001).
53. Neidhardt, F. C., Bloch, P. L. & Smith, D. F. Culture Medium for Enterobacteria. *J Bacteriol* **119**, 736–747 (1974).
54. Tornkvist, M., Larsson, G. & Enfors, S. O. Protein release and foaming in *Escherichia coli* cultures grown in minimal medium. *Bioprocess Eng* **15**, 231–237 (1996).
55. Whitten, A. E., Cai, S. Z. & Trehwella, J. MULCh: modules for the analysis of small-angle neutron contrast variation data from biomolecular assemblies. *J Appl Crystallogr* **41**, 222–226 (2008).
56. Arnold, O. et al. Mantid-Data analysis and visualization package for neutron scattering and mu SR experiments. *Nucl Instrum Meth A* **764**, 156–166 (2014).
57. Wignall, G. D. & Bates, F. S. Absolute Calibration of Small-Angle Neutron-Scattering Data. *J Appl Crystallogr* **20**, 28–40 (1987).
58. Hammouda, B., Ho, D. L. & Kline, S. Insight into clustering in poly(ethylene oxide) solutions. *Macromolecules* **37**, 6932–6937 (2004).
59. Maciejewski, M. W. et al. NMRbox: A Resource for Biomolecular NMR Computation. *Biophys J* **112**, 1529–1534 (2017).

60. Bastidas, M., Gibbs, E. B., Sahu, D. & Showalter, S. A. A primer for carbon-detected NMR applications to intrinsically disordered proteins in solution. *Concept Magn Reson A* **44**, 54–66 (2015).
61. Pervushin, K., Riek, R., Wider, G. & Wuthrich, K. Attenuated T-2 relaxation by mutual cancellation of dipole-dipole coupling and chemical shift anisotropy indicates an avenue to NMR structures of very large biological macromolecules in solution. *P Natl Acad Sci USA* **94**, 12366–12371 (1997).
62. Wittekind, M. & Mueller, L. Hncacb, a high-sensitivity 3d nmr experiment to correlate amide-proton and nitrogen resonances with the alpha-carbon and beta-carbon resonances in proteins. *J Magn Reson Ser B* **101**, 201–205 (1993).
63. Montelione, G. T., Lyons, B. A., Emerson, S. D. & Tashiro, M. An efficient triple resonance experiment using c-13 isotropic mixing for determining sequence-specific resonance assignments of isotopically-enriched proteins. *J Am Chem Soc* **114**, 10974–10975 (1992).
64. Grzesiek, S. & Bax, A. Amino-acid type determination in the sequential assignment procedure of uniformly C-13/N-15-enriched proteins. *J Biomol Nmr* **3**, 185–204 (1993).
65. Lyons, B. A. & Montelione, G. T. An Hccnh triple-resonance experiment using c-13 isotropic mixing for correlating backbone amide and side-chain aliphatic resonances in isotopically enriched proteins. *J Magn Reson Ser B* **101**, 206–209 (1993).
66. Logan, T. M., Olejniczak, E. T., Xu, R. X. & Fesik, S. W. A general-method for assigning nmr-spectra of denatured proteins using 3d Hc(Co)Nh-Tocsy triple resonance experiments. *J Biomol Nmr* **3**, 225–231 (1993).
67. Clowes, R. T., Boucher, W., Hardman, C. H., Domaille, P. J. & Laue, E. D. A 4d Hcc(Co)Nnh experiment for the correlation of aliphatic side-chain and backbone resonances in C-13/N-15 labeled proteins. *J Biomol Nmr* **3**, 349–354 (1993).
68. Carlomagno, T. et al. PLUSH TACSy: homonuclear planar TACSy with two-band selective shaped pulses applied to C-alpha, C' transfer and C-beta, C-aromatic correlations. *J Biomol Nmr* **8**, 161–170 (1996).
69. Muhandiram, D. R. & Kay, L. E. Gradient-enhanced triple-resonance 3-dimensional nmr experiments with improved sensitivity. *J Magn Reson Ser B* **103**, 203–216 (1994).
70. Weisemann, R., Ruterjans, H. & Bermel, W. 3d triple-resonance nmr techniques for the sequential assignment of Nh and N-15 resonances in N-15-labeled and c-13-labeled proteins. *J Biomol Nmr* **3**, 113–120 (1993).
71. Grzesiek, S. & Bax, A. Improved 3d triple-resonance Nmr techniques applied to a 31-Kda protein. *J Magn Reson* **96**, 432–440 (1992).
72. Schleucher, J., Sattler, M. & Griesinger, C. Coherence selection by gradients without signal attenuation - application to the 3-dimensional Hnco experiment. *Angew Chem Int Edit* **32**, 1489–1491 (1993).
73. Kay, L. E., Xu, G. Y. & Yamazaki, T. Enhanced-sensitivity triple-resonance spectroscopy with minimal h2o saturation. *J Magn Reson Ser A* **109**, 129–133 (1994).
74. Zhu, G., Xia, Y. L., Nicholson, L. K. & Sze, K. H. Protein dynamics measurements by TROSY-based NMR experiments. *J Magn Reson* **143**, 423–426 (2000).
75. Lawrence, C. W. & Showalter, S. A. Carbon-Detected 15N NMR spin relaxation of an intrinsically disordered protein: FCP1 dynamics unbound and in complex with RAP74. *J Phys Chem Lett* **3**, 1409–1413 (2012).
76. Loria, J. P., Rance, M. & Palmer, A. G. A. T. R. O. S. Y. CPMG sequence for characterizing chemical exchange in large proteins. *J Biomol Nmr* **15**, 151–155 (1999).
77. Long, D., Liu, M. L. & Yang, D. W. Accurately probing slow motions on millisecond timescales with a robust NMR relaxation experiment. *J Am Chem Soc* **130**, 2432–2433 (2008).
78. Hassan, A. et al. Sensitivity boosts by the CPMAS CryoProbe for challenging biological assemblies. *J Magn Reson* **311** <https://doi.org/10.1016/j.jmr.2019.106680> (2020).
79. Baldus, M., Petkova, A. T., Herzfeld, J. & Griffin, R. G. Cross polarization in the tilted frame: assignment and spectral simplification in heteronuclear spin systems. *Mol Phys* **95**, 1197–1207 (1998).
80. Hong, M. & Griffin, R. G. Resonance assignments for solid peptides by dipolar-mediated C-13/N-15 correlation solid-state NMR. *J Am Chem Soc* **120**, 7113–7114 (1998).
81. Szeverenyi, N. M., Sullivan, M. J. & Maciel, G. E. Observation of spin exchange by two-dimensional fourier-transform C-13 cross polarization-magic-angle spinning. *J Magn Reson* **47**, 462–475 (1982).
82. Takegoshi, K., Nakamura, S. & Terao, T. C-13-H-1 dipolar-assisted rotational resonance in magic-angle spinning NMR. *Chem Phys Lett* **344**, 631–637 (2001).
83. Morcombe, C. R., Gaponenko, V., Byrd, R. A. & Zilm, K. W. 13C CPMAS spectroscopy of deuterated proteins: CP dynamics, line shapes, and T1 relaxation. *J Am Chem Soc* **127**, 397–404 (2005).
84. Shemetov, A. A., Oliinyk, O. S. & Verkhusha, V. V. How to increase brightness of near-infrared fluorescent proteins in mammalian cells. *Cell Chem Biol* **24**, 758 (2017).
85. Day, C. A., Kraft, L. J., Kang, M. & Kenworthy, A. K. Analysis of protein and lipid dynamics using confocal fluorescence recovery after photobleaching (FRAP). *Curr Protoc Cytom* **Chapter 2**, Unit 29 <https://doi.org/10.1002/0471142956.cy0219s62> (2012).
86. Feder, T. J., BrustMascher, I., Slattery, J. P., Baird, B. & Webb, W. W. Constrained diffusion or immobile fraction on cell surfaces: A new interpretation. *Biophys J* **70**, 2767–2773 (1996).
87. Kang, M., Day, C. A., Kenworthy, A. K. & DiBenedetto, E. Simplified equation to extract diffusion coefficients from confocal FRAP data. *Traffic* **13**, 1589–1600 (2012).
88. Schindelin, J. et al. Fiji: an open-source platform for biological-image analysis. *Nat Methods* **9**, 676–682 (2012).
89. Kabsch, W. & Sander, C. Dictionary of protein secondary structure - pattern-recognition of hydrogen-bonded and geometrical features. *Biopolymers* **22**, 2577–2637 (1983).

## Acknowledgements

The authors gratefully acknowledge Aaron Taylor, George Campbell & Victoria Frohlich of the Cell and Tissue Imaging core facility for support of fluorescence microscopy; the members of the St. Jude Children's Research Hospital Center for Advanced Genome Engineering for genome engineering; Dr. Richard Ashmun and the staff of the Flow Cytometry core facility for instructions on the single-cell cloning and cell sorting; the Vector Development and Production Shared Resource for lentiviral production; the staff of the Hartwell Center for Sanger DNA sequencing and STR profiling. The St. Jude Children's Research Hospital core facilities are supported by NCI Cancer Center Support Grant P30 CA021765 and by ALSAC. We acknowledge funding support, as follows: NIGMS grant 5R35GM131891 to R.K., Research Collaborative grant on the Biophysics of RNP Granules from St. Jude Children's Research Hospital to R.K., NIGMS grant 1F32GM133078 to E.B.G., and a Gephardt Endowed Postdoctoral Fellowship from St. Jude Children's Research Hospital to E.B.G. A portion of this research used resources at the Spallation Neutron Source, a DOE Office of Science user facility operated by the Oak Ridge National Laboratory.

## Author contributions

E.G. and R.K. conceived the project. E.G., Q.M., M.F., A.P., S.M., C.S., B.P., and R.K. designed the experiments. E.G., Q.M., M.F., R.B., A.H., G.N., W.L., W.H., C.S., B.P. performed experiments and analyzed data. E.G., Q.M., M.F., A.H.P., S.M., B.P., and R.K. wrote the paper. All authors discussed the results and commented on the manuscript.



## Competing interests

The authors declare no competing interests.

## Additional information

**Supplementary information** The online version contains supplementary material available at <https://doi.org/10.1038/s41467-024-53904-z>.

**Correspondence** and requests for materials should be addressed to Richard Kriwacki.

**Peer review information** *Nature Communications* thanks Marc Baldus, Jason Weber and the other, anonymous, reviewers for their contribution to the peer review of this work. A peer review file is available.

**Reprints and permissions information** is available at <http://www.nature.com/reprints>

**Publisher's note** Springer Nature remains neutral with regard to jurisdictional claims in published maps and institutional affiliations.

**Open Access** This article is licensed under a Creative Commons Attribution-NonCommercial-NoDerivatives 4.0 International License, which permits any non-commercial use, sharing, distribution and reproduction in any medium or format, as long as you give appropriate credit to the original author(s) and the source, provide a link to the Creative Commons licence, and indicate if you modified the licensed material. You do not have permission under this licence to share adapted material derived from this article or parts of it. The images or other third party material in this article are included in the article's Creative Commons licence, unless indicated otherwise in a credit line to the material. If material is not included in the article's Creative Commons licence and your intended use is not permitted by statutory regulation or exceeds the permitted use, you will need to obtain permission directly from the copyright holder. To view a copy of this licence, visit <http://creativecommons.org/licenses/by-nc-nd/4.0/>.

© The Author(s) 2024